NEUTRON SCATTERING INVESTIGATIONS OF PROTON DYNAMICS OF WATER AND HYDROXYL SPECIES IN CONFINED GEOMETRIES

S.-H. CHEN[1*] and C.-K. LOONG[2]
[1]Department of Nuclear Science and Engineering,
Massachusetts Institute of Technology, Cambridge, MA 02139, USA
[2]Intense Pulsed Neutron Source Division,
Argonne National Laboratory, Argonne, IL 60439, USA
[*]Corresponding author, E-mail : sowhsin@MIT.EDU

Received March 31, 2006

This article presents a brief overview of an important area of neutron scattering: the general principles and techniques of elastic, quasielastic and inelastic scattering from a system composed predominately of incoherent scatterers. The methodology is then applied to the study of water, specifically when it is confined in nanometer-scale environments. The confined water exhibits uniquely anomalous properties in the supercooled state. It also nourishes biological functions, and supports essential chemical reactions in living systems. We focus on recent investigations of water encapsulated in nanoporous silica and carbon nanotubes, hydrated water in proteins and water or hydroxyl species incorporated in nanostructured minerals. Through these scientific examples, we demonstrate the advantages derived from the high sensitivity of incoherent neutron spectroscopy to hydrogen atom motions and hydrogen-bond dynamics, aided by rigorous data interpretation method using molecular dynamics simulations or theoretical modelling. This enables us to probe the inter-/intramolecular vibrations and relaxation/diffusion processes of water molecules in a complex environment.

KEYWORDS : Incoherent Neutron Scattering Spectroscopy, Dynamic of Water in Confined Geometry, Supercooled Water, Second Critical Point of Water, Dynamics of Water Near Hydrophilic and Hydrophobic Surfaces, Hydroxyl Ions in Apatite Crystals in Bones

1. INTRODUCTION

Water is a substance intimately connected to life on Earth and even in the cosmos. All life on Earth, humans included, are aqueous beings. Water is present in the cells of all organisms, albeit in various configurations such as being confined to surface of proteins, compartmented between lipid bilayers, or packaged around DNAs, concertedly supporting all kinds of biological functions - from growth to reproduction - in a highly regulated manner. All life on Earth is surrounded in an aqueous environment. Water continually changes from one form to another via the hydrologic cycle - from supercooled droplets in the clouds to surface and underground waters to evaporated vapors - via intricate pathways and mechanisms. Water is also essential to the wellbeing of societies and their citizens. Optimal utilization of water is important to technology, including the nuclear industry. For example, a nuclear power reactor cooled by supercritical water attains a 30% higher thermal efficiency than boiling water reactors [1]. In the case of underground storage of nuclear wastes, the waste containers are to be surrounded by a clay buffer that will absorb the natural water from the rocks, swell, and eventually form a barrier to seal the containers permanently from contact with groundwater [2]. However, if the containers may eventually be bleached by corrosion - not an unrealistic scenario over a period of as long as 10,000 years, then the transport of water confined between the clay platelets as well as possible exchange of radioactive ions or complexes in the waste with those in the clay have to be understood [3].

While many methods can be used to measure the macroscopic properties of water inside biological, geological and engineering systems, experimental techniques capable of determining the structure and dynamics of water molecules under nanometer-scale confinement are scarce. Neutron scattering is a method of choice because of the extraordinary large neutron incoherent scattering cross section of hydrogen atoms, rendering high sensitivity to hydrogen motion unmatched by optical and x-ray spectro-

scopies [4]. Furthermore, judicious H-D substitution or application of high magnetic fields and neutron polarization analysis can enhance significantly the contrast between targeted hydrogen groups against the host medium for structural determination. The spatiotemporal range of neutron scattering encompasses the 0.01-100 nm and 10^{-4}-10 ns realm that matches well the length and time scale of short-to-long range order structure, molecular diffusion and atomic vibrations in water. Additionally, the measured neutron spectra, as Fourier transforms of particle-particle space-time correlation functions, can afford quantitative comparisons in a straightforward manner with those calculated by computer simulations or theoretical modelling.

Having enumerated the important areas of confined water in life, environment, and engineering which obviously are too vast to be adequately covered in depth or in breadth in a single paper, we hasten to confine the scope of this article to include water encapsulated in nanoporous silica and carbon nanotubes as well as water associated with proteins and adsorbed in nanostructured minerals. Section II introduces the formulae of neutron scattering functions and their physical interpretations. Examples of confined or adsorbed water in selected systems are given in Section III, each with a brief description of scientific motivation, followed by presentation of the neutron data, and discussion of the results. Section IV presents some concluding remarks.

2. NEUTRON SCATTERING STUDIES OF MOLECULAR DYNAMICS OF WATER

2.1 Incoherent Elastic, Quasi-elastic and Inelastic Scattering

Quasi-elastic neutron scattering (QENS) and inelastic neutron scattering (INS) techniques offer many advantages for the study of single particle dynamics of water. The main reason is that the total scattering cross section of hydrogen is much larger than that of atoms in for example silica or carbon, composed of oxygen and silicon or carbon. Furthermore, the neutron scattering of hydrogen atoms is mostly incoherent so that QENS and INS spectra reflect, essentially, the self-dynamics of the hydrogen atoms in water. Combining this dominant cross section of hydrogen atoms with the use of spectrometers having different energy resolutions, we can study the molecular dynamics of water in a wide range of time-scale, encompassing picoseconds to tens of nanoseconds. In addition, investigating different Q values (Q being the magnitude of the exchanged wave vector) in the range from $0.2 \leq Q \leq 2.0$ Å^{-1}, the spatial characteristics of water dynamics can be investigated at the sub-nanometer level.

In a typical QENS or INS experiment, one sends in a monochromatic neutron beam with an incident energy E_i and wave vector $\vec{k}_i$ to the sample and detect the scattered neutrons with a final energy in an energy interval (E_f,E_f +dE_f) and an average final wave vector $\vec{k}_f$ by a neutron detector subtending a solid angle $d\Omega=\sin\theta d\theta d\varphi$, where θ is a scattering angle. One then computes, from the scattered intensity $I_s(E_f,\theta)$ and the incident flux $I_i(E_i)$, the double differential scattering cross section $\sigma_s(E_i \rightarrow E_f,\theta) = \frac{d^2\sigma_s}{d\Omega dE} = \frac{I_s(E_f,\theta)r^2}{I_i(E_i)}$, where r is the distance between the sample and the detector. In the case of incoherent scattering from hydrogen atoms, the incoherent scattering cross section of a hydrogen atom σ_H dominates the scattering signal because the hydrogen cross section is ten times larger than all the other atoms. For this case, it can be shown generally [5] that the double differential scattering cross section is $\frac{d^2\sigma_H}{d\Omega dE}$ proportional to the self-dynamic structure factor of hydrogen atoms $S_H(Q,E)$ through the following relation:

$$\frac{d^2\sigma_H}{d\Omega dE} = N\frac{\sigma_H}{4\pi\hbar}\frac{k_f}{k_i}S_H(Q,E), \qquad (1)$$

where $E = E_i - E_f = \hbar\omega$ is the energy transferred by the neutron to the sample; $\hbar\vec{Q} = \hbar\vec{k}_i - \hbar\vec{k}_f$, the momentum transferred in the scattering process; and N, the number of scattering centers in the scattering volume. The dynamic structure factor, $S_H(Q,E)$, which embodies the elastic, quasi-elastic and inelastic scattering contributions, is proportional to the probability that a neutron transfers a momentum $\hbar\vec{Q}$ and an energy $E = \hbar\omega$ in the scattering process. It can be expressed as a Fourier transform of the self Intermediate Scattering Function (ISF) of the hydrogen atom, $F_H(Q,t) = \exp\{i\vec{Q}\cdot[\vec{r}(t) - \vec{r}(0)]\}$, according to the equation:

$$S_H(Q,\omega) = \frac{1}{2\pi}\int_{-\infty}^{\infty} dt e^{-i\omega t}F_H(Q,t). \qquad (2)$$

In this equation, we use a notation $S_H(Q,E) = \hbar S_H(Q,\omega)$, the alternative notation of which we shall use in the subsequent sections. $F_H(Q,t)$ is the density-density time correlation function of the tagged hydrogen atom being measured by the neutron scattering. It is, thus, the primary quantity of theoretical interest related to the experiment. It can be calculated by a model, such as Relaxing-Cage Model (RCM), and a molecular dynamics (MD) simulation based on a phenomenological potential model of water.

2.1.1 Elastic Scattering (ω= 0)

For analysis of the elastic incoherent-scattering intensity from hydrogen atoms when they are bound in space, it can be shown that

$$S_H(Q,0) = Be^{-\langle u_H^2\rangle Q^2}, \quad (3)$$

where $\langle u_H^2 \rangle$ is the mean-square displacement of the hydrogen atoms and B, a constant. Therefore, $\langle u_H^2 \rangle$ can be determined experimentally by fitting the integrated elastic intensities from the incoherent scattering collected by many detectors over a Q range with the above equation.

2.1.2 Quasi-Elastic Scattering ($\omega \neq 0$)

The QENS data analysis method is presented in the next subsection. In principle, the full dynamics of bulk or confined water should include both the translational and the rotational motions of a rigid water molecule. Given the fact that in the process of QENS data analysis, we only focus our attention to ISF with $Q \leq 1.1$ Å^{-1}, we can safely neglect the contribution of rotational motion to the total dynamics [6], which means $F_H(Q,t) \approx F_T(Q,t)$, where $F_T(Q,t)$ is the translational part of the ISF.

2.1.3 Inelastic Scattering ($\omega \neq 0$)

For analysis of the inelastic-scattering intensity dominated by incoherent scattering from hydrogen atoms, the neutron-weighted vibrational density-of-states (DOS) of hydrogen atoms can be approximated by

$$G_H(E) = \frac{2M_H}{\hbar^2}\frac{E}{n(E)+1}\left\langle \frac{e^{\langle u_H^2\rangle Q^2}}{Q^2} S(Q,E)\right\rangle. \quad (4)$$

where M_H is the mass of hydrogen atom and $n(E)$ is the Bose-Einstein distribution function, and $\langle ... \rangle$ represents the average over all observed Q values.

2.2 Relaxing-Cage Model (RCM) of the Single-Particle Dynamics of Water

During the past several years, we have developed the Relaxing-Cage Model (RCM) for the description of translational and rotational dynamics of water at supercooled temperatures. This model has been tested with MD simulations of SPC/E water, and has been found to be accurate. It has been used to analyze many QENS data from supercooled bulk water as well as interfacial water [7-11].

On lowering the temperature below the freezing point, around a given water molecule, there is a tendency to form a hydrogen-bonded, tetrahedrally coordinated first and second neighbor shells (cage). At short times, less than 0.05 *ps*, the center of mass of a water molecule performs vibrations inside the cage. At long times, longer than 1.0 *ps*, the cage eventually relaxes and the trapped particle can migrate through the rearrangement of a large number of particles surrounding it. Therefore, there is a strong coupling between the single particle motion and the density fluctuations of the fluid. The mathematical expression of this physical picture is the so-called Relaxing-Cage Model.

The RCM assumes that the short-time translational dynamics of the tagged (or the trapped) water molecule can be treated approximately as the motion of the center of mass in an isotropic harmonic potential well provided by the mean field generated by its neighbors. We can, then, write the short time part of the translational ISF in the Gaussian approximation, connecting it to the velocity auto-correlation function, $\langle \vec{v}_{CM}(t) \cdot \vec{v}_{CM}(0) \rangle$, in the following way:

$$\begin{aligned} F_T^s(Q,t) &= \exp\left\{-Q^2\frac{\langle r_{CM}^2(t)\rangle}{2}\right\} \\ &= \exp\left\{-Q^2\left[\int_0^t (t-\tau)\langle \vec{v}_{CM}(0)\cdot\vec{v}_{CM}(\tau)\rangle d\tau\right]\right\} \end{aligned} \quad (5)$$

Since the translational density of states, $Z_T(\omega)$, is the time Fourier transform of the normalized center of mass velocity auto-correlation function, one can express the mean squared deviation, $\langle r^2_{CM}(t) \rangle$, as follows:

$$\left\langle r_{CM}^2(t)\right\rangle = \frac{2}{3}\left\langle v_{CM}^2\right\rangle \int_0^\infty d\omega \frac{Z_T(\omega)}{\omega^2}\left(1-\cos\omega t\right). \quad (6)$$

where $\langle v^2_{CM} \rangle = \langle v_x^2 \rangle + \langle v_y^2 \rangle + \langle v_z^2 \rangle = 3v_o^2 = 3k_BT/M$ is the average center of mass square velocity, and M is the mass of water molecule.

Experiments and MD results show that the translational harmonic motion of a water molecule in the cage gives rise to two peaks in $Z_T(\omega)$ at about 10 and 30 meV, respectively [12]. Thus, the following Gaussian functional form is used to represent approximately the translational part of the density of states:

$$\begin{aligned} Z_T(\omega) = (1-C)\frac{\omega^2}{\omega_1^2\sqrt{2\pi\omega_1^2}}\exp\left[-\frac{\omega^2}{2\omega_1^2}\right] \\ + C\frac{\omega^2}{\omega_2^2\sqrt{2\pi\omega_2^2}}\exp\left[-\frac{\omega^2}{2\omega_2^2}\right] \end{aligned} \quad (7)$$

Moreover, the fit of MD results using Eq. (7) gives C = 0.44, ω_1 = 10.8 THz and ω_2 = 42.0 THz.

Using Eqs. (5-7), we finally get an explicit expression for $F_T^s(Q,t)$:

$$F_T^s(Q,t) = \exp\left\{-Q^2 v_0^2 \left[\frac{1-C}{\omega_1^2}\left(1-e^{-\omega_1^2 t^2/2}\right) + \frac{C}{\omega_2^2}\left(1-e^{-\omega_2^2 t^2/2}\right)\right]\right\}. \quad (8)$$

Eq. (8) is the short-time behavior of the translational ISF. It starts from unity at $t = 0$ and decays rapidly to a flat plateau determined by an incoherent Debye-Waller factor $A(Q)$, given by:

$$A(Q) = \exp\left\{-Q^2 v_0^2 \left[\frac{1-C}{\omega_1^2} + \frac{C}{\omega_2^2}\right]\right\} = \exp\left[-Q^2 a^2/3\right] \quad (9)$$

where a is the root mean square vibrational amplitude of the water molecules in the cage, in which the particle is constrained during its short-time movements. According to MD simulations, $a \approx 0.5$ Å is fairly temperature independent [13].

On the other hand, the cage relaxation at long-time can be described by the standard α-relaxation model, according to the Mode-Coupling Theory (MCT), with a stretched exponential having a structural relaxation time τ_T and a stretch exponent β. Therefore, the translational ISF, valid for the entire time range, can be written as a product of the short time part and a long time part:

$$F_T(Q,t) = F_T^s(Q,t)\exp\left[-(t/\tau_T)^\beta\right] \quad (10)$$

The fit of the MD generated $F_T(Q,t)$ using Eq. (10) shows that τ_T is Q- dependent, obeying the power-law:

$$\tau_T = \tau_0 (aQ)^{-\gamma}, \quad (11)$$

where γ is ≤ 2, with a slight dependency on Q, and $\beta < 1$ is slightly Q dependent as well. In the $Q \rightarrow 0$ limit, one should approach the diffusion limit, where $\gamma \rightarrow 2$ and $\beta \rightarrow 1$. Thus the translational ISF can be written as: $F_T(Q,t) = \exp[-DQ^2 t]$, D being the self-diffusion coefficient. In QENS experiments, this low Q limit is not usually reached, and both β and γ can be considered Q independent in the limited Q range of $0 \leq Q \leq 1$ [9,10].

We define a Q-independent average translational relaxation time

$$\langle \tau_T \rangle = (\tau_0/\beta)\Gamma(1/\beta), \quad (12)$$

which is convenient quantity to be extracted from the experimental data by the fitting process of RCM. This quantity can be identified to be proportional to the α-relaxation time which dominates the long-time decay of the ISF in low temperature water. Combining Eqs. (1), (8) and (10), we can calculate the theoretical values of $S_H(Q,\omega)$ and compare it directly with its experimental spectral data.

2.3 Methods of Neutron Spectroscopy

QENS and INS measurements were performed using the High-Flux Backscattering Spectrometer (HFBS) and the Disc-Chopper Spectrometer (DCS) at the NIST Center for Neutron Research (NCNR), and the High-Resolution Medium-Energy Chopper Spectrometer (HRMECS) and the Quasielastic Neutron Spectrometer (QeNS) at the Intense Pulsed Neutron Source (IPNS) of Argonne National Laboratory. Recalling the fact that 1 meV is equivalent to 11.6 K, neutron spectroscopy can be subdivided into cold, thermal, and epithermal neutron scattering according to the energy transfer E with loose respective boundaries of 1-8, 8-80 and above 80 meV. The reactor-based spectrometers at NCNR use cold neutrons generated by the reactor cold source to attain the best energy resolution: ~0.8 μeV for HFBS [14] to ~20 μeV for DCS [15], which is essential to the measurements of slow dynamics, i.e., relaxation and diffusion processes in low-temperature water. IPNS, on the other hand, is an accelerator-based spallation source, which always undermoderate the neutrons even with cryogenic moderators in use. Thus the plentiful epithermal neutrons benefit a complete measurement of intermolecular and intramolecular vibrational modes extending to hundreds of meV using the IPNS instruments. HRMECS [16], being a direct-geometry time-of-flight spectrometer operating at fixed (selected) incident neutron energy E_i, yields an energy resolution $\Delta E/E_i$ varying from about 4 % at the elastic region to about 2 % near the end of the neutron energy-loss spectrum. Therefore, by choosing different incident energies, e.g., 50, 140 and 600 meV, the entire inter- and intramolecular vibrational spectrum of water can be measured with good resolution. QeNS is a crystal-analyzer spectrometer covering a dynamic range of 0-100 meV with $\Delta E/E$= 4-5 % and an elastic resolution of 80 μeV.

All the spectrometers are equipped with detectors covering a wide range of scattering angles which enable simultaneous data collection at different wave vectors. A specific sample environment with respect to temperature, pressure, atmosphere, etc., is maintained and controlled by a proper ancillary equipment. The background scattering, such as from a sample holder or from a dry sample, was removed by subtracting the corresponding empty-holder and dry-sample run from the overall dataset. Measurements of neutron standards (vanadium, D_2O, Cd absorber, etc.) provided incident-spectrum normalization, detector calibra-

tion and correction for sample attenuation.

2.4 QENS Data Analysis

When we use RCM to analyze spectra from QENS experiments, we usually observe an additional presence of a pronounced elastic component superimposed on the top of quasielastic broadening [11]. The presence of this elastic component is clearly detectable at most temperatures and Qs, even with the broader resolution of DCS.

Defining the magnitude of the wave vector transfer Q, corresponding to the scattering angle θ at the elastic channel as $Q_0 = {}^{[4\pi \sin(\theta/2)]}/_{\lambda}$, we can analyze the experimental data according to the following model:

$$S(Q,\omega) = pR(Q_0,\omega) + (1-p)FT\{F_H(Q,t)R(Q_0,t)\}, \quad (13)$$

where p is the fraction of the elastic component, $F_H(Q,t) \approx F_T(Q,t)$ is the ISF of hydrogen atoms which defines the quasielastic scattering, $R(Q_0,t)$ is the experimental resolution function, and the symbol FT denotes the Fourier transform from time t to frequency ω.

Taking the weight of the elastic component p as a fitting parameter, we obtain the temperature dependent values for p. However, in this way we were trying to evaluate contributions from: (i) the hydrogen atoms of surface silanol groups in the silica materials [17]; and (ii) the water molecules interacting strongly with surface silanol groups via hydrogen bonds.

For temperatures lower than 270 K, the fraction of the elastic component seems to increase, whereas for $T \geq 270$ K a plateau is reached. The fast increase as lowering temperature is obviously connected to the slowing down of water dynamics near the surface. In the mean time, the plateau value is then the scattering due to the hydrogen atoms of surface silanol groups. The surface silanol groups are so well organized and strong that they may be seen as temperature independent. For this reason, to obtain consistent results and only take into account the contribution from the surface silanol groups as the elastic component, we have fixed p to its plateau value at high temperatures [11], when analyzing the data from different spectrometers.

3. SCIENTIFIC EXAMPLES

3.1 Fragile-to-Strong Transition in Supercooled Water Confined in Nanoscale Porous Silica Materials

Glass is an amorphous solid form of matter that results when a fluid is supercooled or compressed in such a way that it bypasses crystallization. Many types of materials are capable of glass formation, such as molecular liquids, polymers, metal alloys and molten salts. Given such diversity of materials, a general scheme, by which different glass-forming materials can be systematically classified according to their relaxational behaviors, is useful. One such scheme is the classification of glass-formers according to their 'fragility'. Fragility measures the rate with which transport properties of a liquid, such as structural relaxation time τ_T, viscosity η or the inverse self-diffusion constant $1/D$, change as the glassy state is approached from the liquid side by lowering temperature.

By convention, the glass transition temperature T_g is where the viscosity η reaches a value of 10^{12} Pascal-second (Pa-s) or the structural relaxation time τ_T reaches an order of 100 second. The approach to this large η or τ_T, however, differs from one liquid to another. When displayed in an Arrhenius plot of log η (or log τ_T) versus inverse temperature $1/T$, some liquids (such as silica) show a steady, linear increase, while others display a much steeper dependence on $1/T$ (such as *o*-Terphenyl). The former are called 'strong' liquids, and the latter, 'fragile' liquids. Thus, the glassy liquid is called 'fragile' when its viscosity or relaxation time varies according to super-Arrhenius law, such as the Vogel-Fulcher-Tammann (VFT) law:

$$\tau_T = \tau_1 e^{DT_0/(T-T_0)} \quad (14)$$

where T_0 is the temperature of an apparent divergence of the relaxation time (or sometime called Kauzmann temperature); the magnitude of D gives the degree of fragility; and τ_1 is a prefactor related to microscopic vibrational relaxation time inside the cage forming by neighbors in the liquid state. The liquid is called 'strong' when the viscosity or relaxation time obeys Arrhenius law:

$$\tau_T = \tau_1 e^{E_A/RT} \quad (15)$$

where E_A is the energy barrier for the relaxation process and R, the gas constant [18].

For water, which is a fragile liquid at room temperature and at moderately supercooled temperatures, Angell and coworkers [19] proposed that a 'fragile-to-strong' transition would occur at around 228 K at ambient pressure, based on a thermodynamic argument. But supercooled water nucleates into hexagonal ice at and below $T_H = 235$ K, so this transition lies in an inaccessible region of temperatures and it has not been observed directly so far [20]. By containing water in small cylindrical pores (pore size $\leq$ 18 Å) of MCM-41-S, we were able to circumvent the homogenous nucleation process and supercool water down to 160 K.

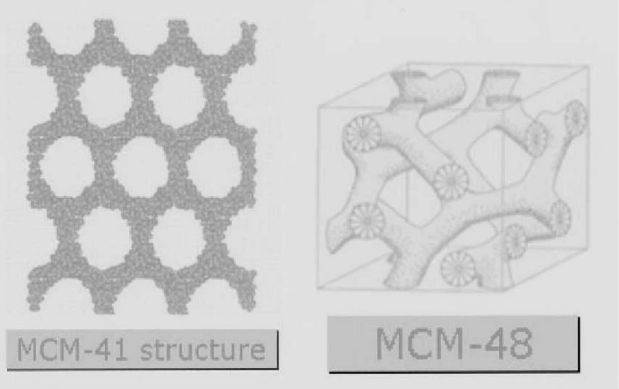

Fig. 1. Microscopic structures of MCM-41-S and MCM-48-S

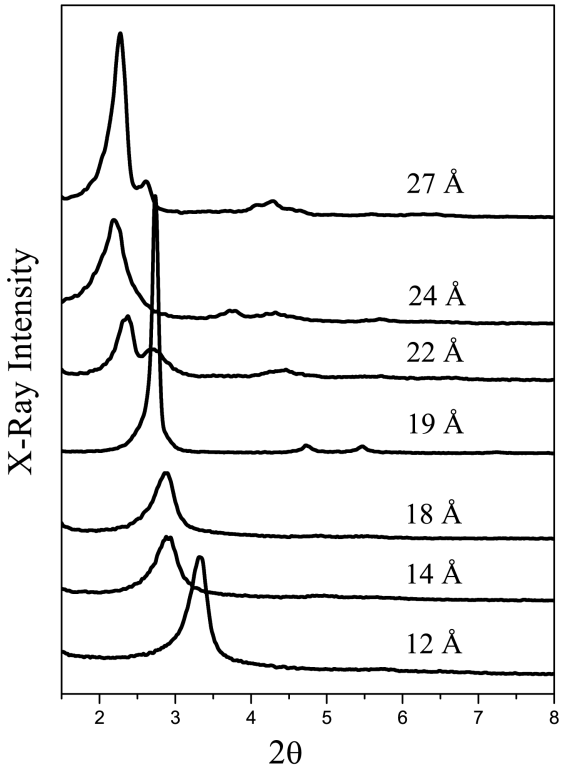

Fig. 2. This figure shows XRD patterns of MCM-41-S samples with different pore sizes taken at room temperature and ambient pressure. The sharp XRD peaks show that the samples are well-ordered. The (1 0 0) peak (the highest peak) is related to the d-spacing according to the rule : $2d \sin(\theta) = \lambda$, where λ = 1.54 Å and θ is in degree. Since the samples do not show a peak at the high angle region, it means that we have just one phase (pure phase). The number above each curve indicates the average pore diameter of that sample.

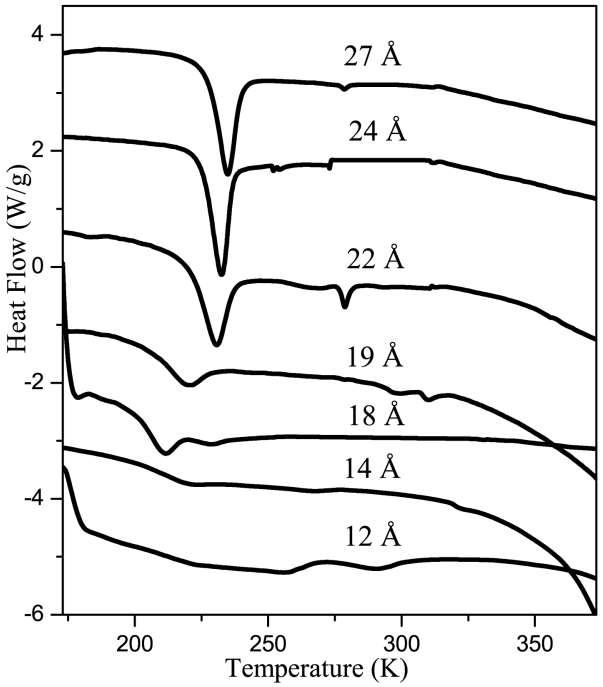

Fig. 3. DSC curves of water inside MCM-41-S samples having different pore sizes (indicated by the numbers above the curves). The sharp negative-going peaks signal the freezing temperatures. It is noted that the samples with pore size ≤ 18 Å do not show an obvious freezing peak.

3.1.1 Sample Characterization

We did experiments initially with two kinds of samples having different pore geometries, MCM-41-S and MCM-48-S, to extract most of our results and compare with RCM prediction and MD simulation results. Fig. 1 shows the schematic microstructures of MCM-41-S and MCM-48-S. The former matrix has 1-D cylindrical tubes arranged in a hexagonal structure whereas the latter has a 3-D bicontinuous morphology.

In this section, we discuss only the case of MCM-41-S nanoporous silica materials, which is synthesized by using copolymer micelles in its cylindrical liquid crystalline phase as a template. Similar to synthesizing MCM-48-S [21], to make the mesoporous materials together with short surfactant (C_{12}TMAB), we employed small quaternary ammonium ions, TEAOH, to separately develop zeolitic nanocluster as silica precursor. In this way, we will get MCM-41-S with smaller pore sizes and stronger silica walls than traditional ways [22-24].

The synthesized samples have been characterized using x-ray powder diffraction (XRD), nitrogen adsorption-desorption and differential scanning calorimetry (DSC).

The XRD patterns of the samples show that the MCM-41-S had hexagonal (P6mm) symmetry, as shown in Fig. 2. All the samples exhibit high hydrothermal stability.

The melting/freezing behavior of water in the samples (fully hydrated) has been checked by DSC measurements. According to the Gibbs-Thomson equation, the melting point of small crystal is proportional to the crystal size, which, in this case, is equal to the pore size of the material. Thus, one expects the liquid state of water would persist to very low temperature if the pore size can be made sufficiently small. In Fig. 3, the DSC curve shows the melting points which are specified by the temperatures at the positions of the inverted peaks. For samples with pore size $\geq$ 19 Å, we do see a small peak near 0°C which is due to the water outside the nanochannel (unconfined). For samples having pore sizes $\leq$18 Å, we do not see any abrupt melting transition near 0°C, indicating that there is no water residing outside the channel. Furthermore, the water inside the channel does not freeze all the way down to 180 K.

3.1.2 Motivation

The interest of the scientific community for the properties of water confined in nanoporous matrices at supercooled temperatures has a twofold basis. On the one hand, confining water in nanometric cavities allows us to study water in deeply supercooled states. This temperature range is of fundamental importance to science of water. At ambient pressure, bulk liquid water shows an anomalous increase of thermodynamic quantities and an apparent divergent behavior of transport properties, on approaching the singular temperature T_c = 228 K [25], which lies below the homogenous nucleation temperature T_H. Thus, there is a lack of experimental data in this temperature range, which hampers the verification or the rejection of the different physical pictures proposed to explain the origin of the anomalous behavior of water. On the other hand, in many real life systems water is not in its bulk form but is located near surfaces or contained in small cavities. It is the case, for example, for water in rocks, in polymer gels, and in biological membranes [26]. In addition, the properties of water in porous silica glasses, such as Vycor, and silica gel, are relevant in catalytic and separation processes. The above two lines of interests are obviously closely related, as the clarification of the fundamental properties of water is likely to be the key for understanding the behavior of many real life systems. For example, in the case of enzymatic activity of protein, it has been found that the onset of protein activities is strongly correlated to the onset of orientational fluctuations that initiate structural rearrangements within the transient H-bond water network surrounding the protein [27,28]. Therefore, the study of the dynamics of water confined in nano-pores as a function of temperature and pressure is relevant in understanding important effects in systems of interest in biology, chemistry, and geophysics [29,30].

Due to the facts mentioned above, both the structure and dynamics of water in confined geometries have been widely studied using MD simulations and different experimental techniques. MD simulations of the extended simple point charge (SPC/E) model of bulk water have furnished relevant results for understanding the dynamics of supercooled water [13,31-34]. From the analysis of these results, the RCM for the translational and rotational dynamics of water at supercooled temperatures have been developed [31,32]. In addition to this, MD simulations of SPC/E water confined in silica nanopores have been carried out as well [35,36]. The interaction between the hydrophilic surface and the water molecules has noticeable effects on the structure of the first and second layer of water near the pore surface [17]. As far as the dynamics is concerned, when confined near hydrophilic surfaces, water molecules are in the glassy state. In general, the water molecules show a dynamics similar to that of supercooled water [35,36] at a lower equivalent temperature of some 30 degrees [27,37].

Experimentally, the structural properties of water at supercooled temperatures [38] and in confinement [39] were studied extensively using x-ray and neutron diffraction. On the other hand, the relaxational dynamics of water confined in mesoporous matrices were studied using dielectric spectroscopy [20,40-44] and different nuclear magnetic resonance (NMR) techniques [45-48].

This section presents a systematic investigation of temperature and pressure dependences of dynamics of water inside nanoporous silica materials. The temperature range covers from room temperature down to deeply supercooled states, and the pressure ranges from ambient to 2400 bar. QENS data collected are analyzed according to a single consistent model RCM, which is valid for bulk as well as confined water as was shown by MD simulation [13,31-36].

3.1.3 QENS Experimental Results

The quasielastic broadening has been analyzed according to the RCM as described in the previous section. $F_H(Q,t)$ is described in terms of seven parameters (from Eqs. 1, 8, 10, 11 and 13), C, ω_1, ω_2, τ_0, γ, β and p. Three of them are related to the short-time dynamics, namely C, ω_1 and ω_2. The short-time dynamics is not strongly temperature dependent, according to MD simulation results. On the other hand, the quasielastic broadening is mostly determined by the long-time dynamics. Therefore, the values of C, ω_1 and ω_2 are fixed according to the MD simulation results [11], which were tested by the experimental results from INS with a satisfactory agreement [31,32].

The remaining four parameters, namely p, τ_0, γ, β can then be determined from the analysis of a group of low-Q QENS spectra. We report the results of our analysis with the values of p fixed to their plateau values.

We show in Fig. 4, as an example, two sets (temperature series) of QENS area-normalized spectra taken at HFBS and DCS spectrometers. As can be seen, RCM analysis

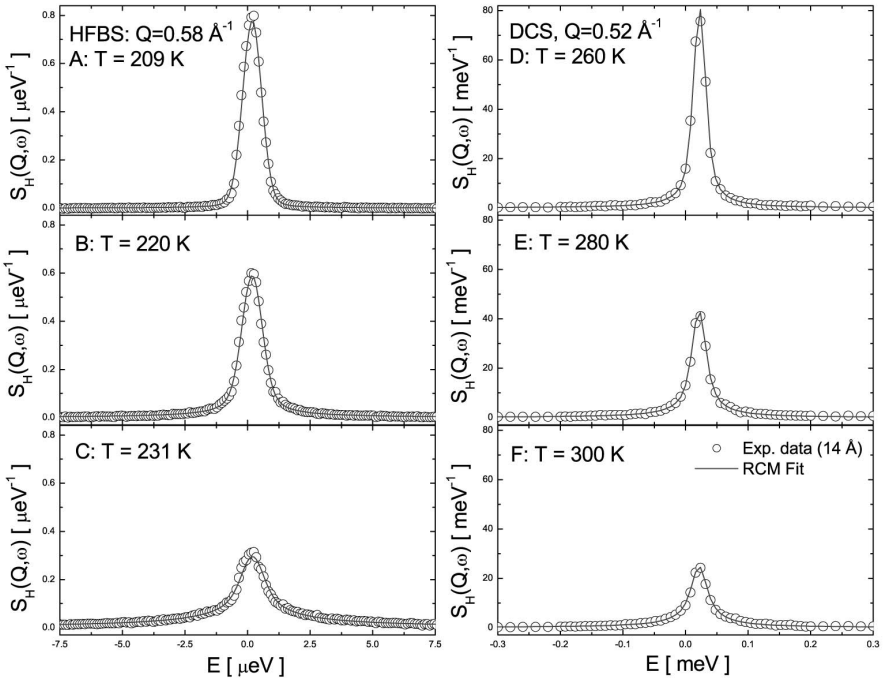

Fig. 4. This typical QENS spectra of hydrated MCM-41-S-14 sample show that RCM analysis agrees well with experimental data. The left-hand panels show the spectra taken from HFBS with resolution of 0.8 μeV. The right-hand panels are the data taken from DCS with resolution of 20 μeV. The solid circles are the experimental data; the continuous lines, the RCM fit.

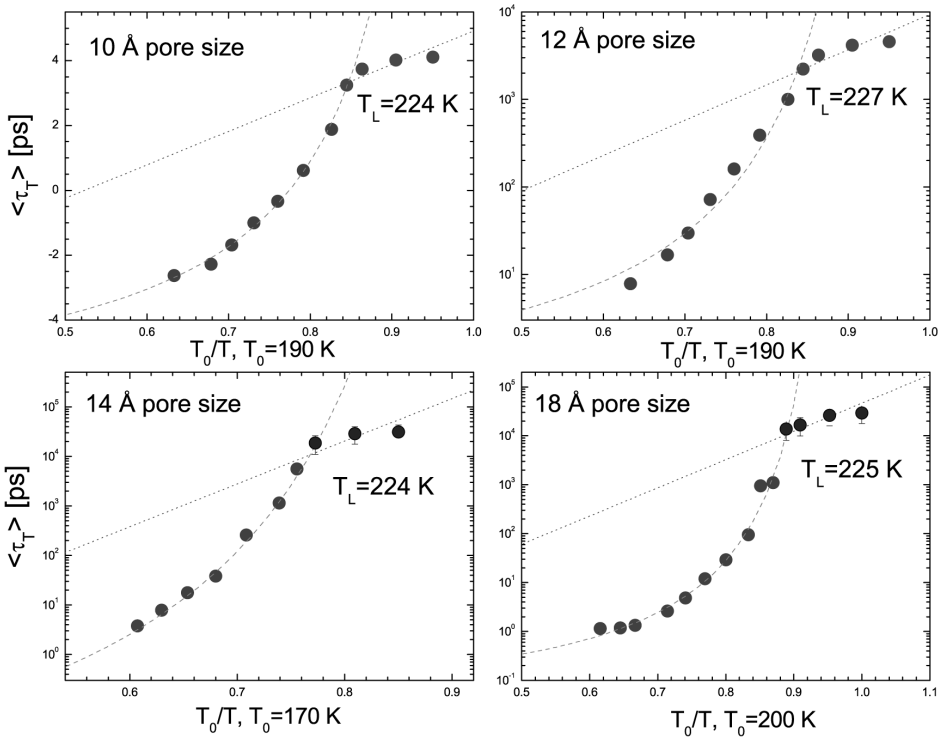

Fig. 5. Temperature dependence of $\langle\tau_T\rangle$ plotted in log ($\langle\tau_T\rangle$) vs T_0/T scale. Data at ambient pressure from H_2O confined in MCM-41-S with different pore sizes are shown in different panels. Solid circles are the experimental data; the dash lines are the VFT law fit of the experimental data; and the dotted lines are the Arrhenius law fit of the experimental data.

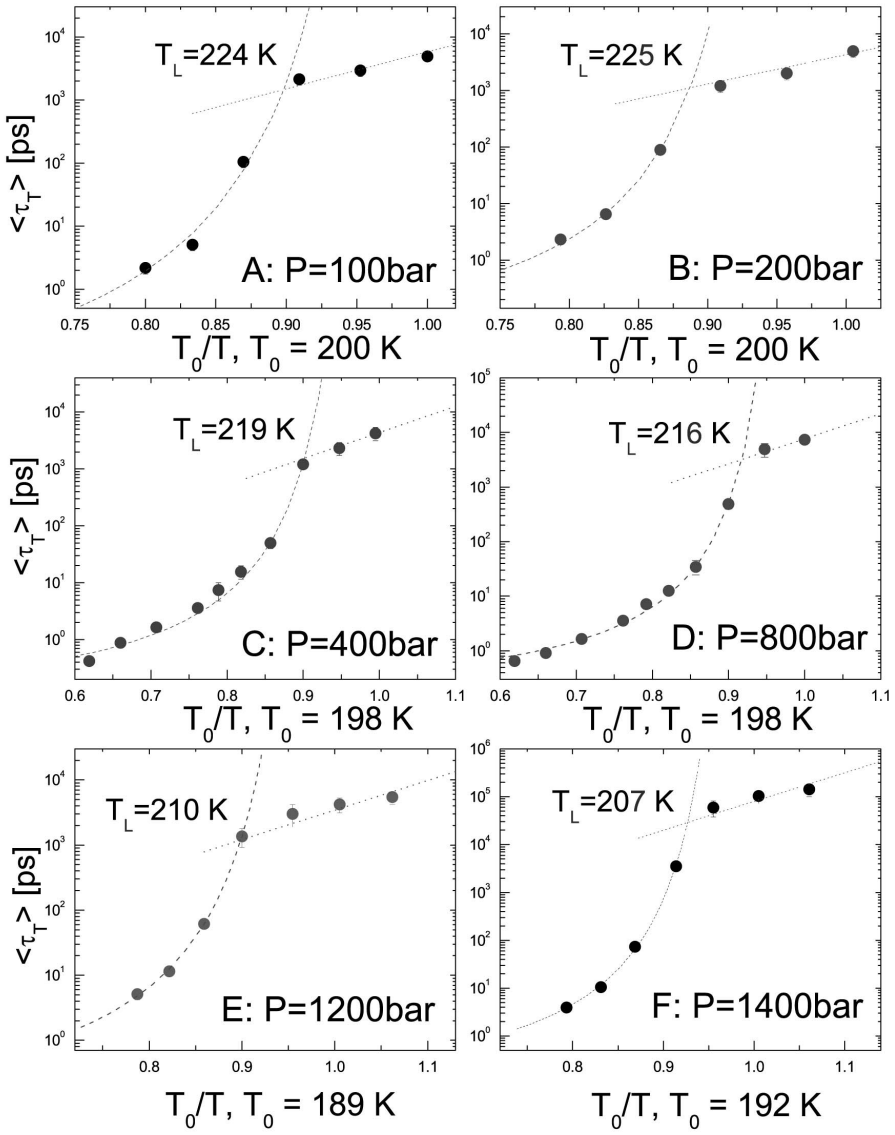

Fig. 6. Summary of the data from pressure range where a well-defined fragile-to-strong crossover is observed. Temperature dependence of $\langle\tau_T\rangle$ plotted in log ($\langle\tau_T\rangle$) vs T_0/T scale. Data from 100, 200, 400, 800, 1200, 1400 bars are shown in panels A, B, C, D, E and F, respectively.

agrees well with experimental spectra in all investigated cases. It is remarkable that using four parameters we were able to reproduce the data from 9 (DCS), and 7 (HFBS) constant-angle spectra. On the other hand, it is clearly shown in the figure that the quasielastic broadening is strongly temperature dependent. The width of the peak is progressively sharpened as temperature is lowered. Thus $T \leq 240$ K, the 0.8 μeV resolution of HFBS is necessary to obtain useful data.

The fitting of the data allowed us to extract parameters describing the translational dynamics of water, and calculate the average translational relaxation time, $\langle\tau_T\rangle$, which will show the FSC phenomenon and that is the central result of this paper.

Fig. 5 shows the temperature dependence of the average translational relaxation times, $\langle\tau_T\rangle = \frac{\tau_0}{\beta}\Gamma(1/\beta)$, where Γ is the gamma function, τ_0 and β are the characteristic relaxa-

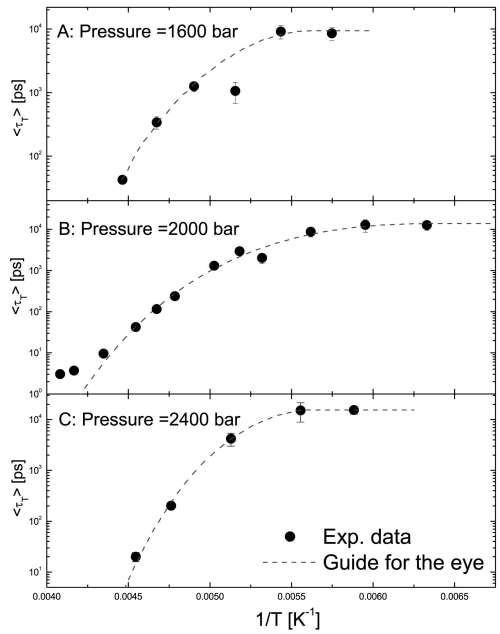

Fig. 7. Summary of the data from pressure range where no well-defined fragile-to-strong crossover is observed. Temperature dependence of $\langle \tau_T \rangle$ plotted in $\log(\langle \tau_T \rangle)$ vs $1/T$ scale. Data from 1600, 2000 and 2400 bars are shown in panels A, B and C, respectively.

tion time and the stretch exponent of the translational dynamics, respectively. The resultant $\langle \tau_T \rangle$ has been fitted to a VFT law, for $T \geq 230$ K, obtaining parameters, D, T_0 and τ_1 for different pore sizes at ambient pressure. A critical law, which is usually used for bulk supercooled water, would fit the data above 240 K, but deviates from the data below 240 K [49]. At $T \leq 225$ K, there is a sudden change in the slope of the $1/T$ dependence of $\log \langle \tau_T \rangle$, which can be fitted with an Arrhenius law. Our best fit to $\langle \tau_T \rangle$ gives us T_0 values in the vicinity of 200 K, and D values around 2 indicating a very fragile liquid. Our finding is in agreement with the known properties of water below the melting point and in the supercooled region. In fact, a fragile-to-strong crossover (FSC) in water was proposed [19] on the basis of the determination of the fragility of water near the melting and glass transition temperatures: near T_g water is a very strong liquid, whereas in the supercooled region it is the most fragile one. A strong experimental support to this hypothesis was already given by a dielectric relaxation investigation of water confined in vermiculite clay [20], although the actual transition was not observed. It is to be noted that the crossover temperature T_L for different pore size samples, reported in Fig. 5, does not change within error bars. Thus we propose that when pore size of confinement is sufficiently small, $\leq$18 Å, the FSC temperature is size-independent, which means that FSC is a universal

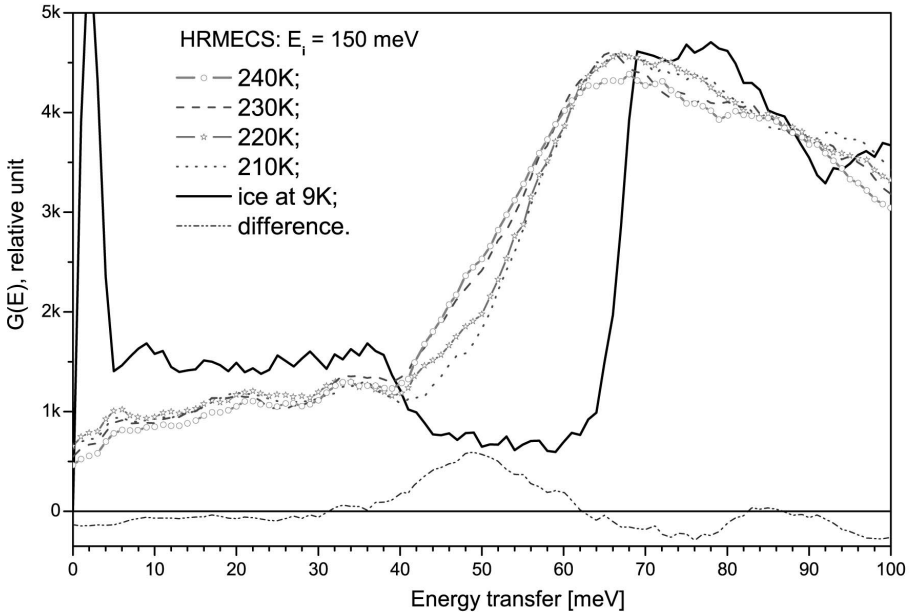

Fig. 8. The generalized librational density of states G(E) (taken with $Q < 2$Å^{-1}) of ice and confined water (within the energy range from 40 meV to 120 meV) at different temperatures measured with HRMECS spectrometer using incident neutron energy of 150 meV. It should be noted that G(E) of ice (solid line) is characterized by a much steeper leaning edge compared to that of supercooled water in the temperature range from 210 K to 240 K. The broader G(E) of supercooled water confined in MCM-41-S with pore diameter of 18 Å is seen to be more characteristic of a liquid state. From the behavior of the low-energy cut-off of the librational band around 50 meV, it is obvious that the state of confined water (its hydrogen bond network) is different at temperatures above and below 225 K. The difference between the average spectra above and below 225 K is shown to have a clear peak at around 50 meV (dash-dot-dot line).

property of supercooled water when the length scale of confinement is of order of nanometer size.

We have already shown that at ambient pressure, for fully hydrated MCM-41-S of pore size ≤ 18 Å, $\langle \tau_T \rangle$ exhibits a FSC with the same crossover temperature $T_L = 225$ K within error bars. In Figs. 6 and 7, we exhibit the temperature variation of $\langle \tau_T \rangle$ for water molecules as a function of pressure. It is seen that the panels in Fig. 6 all show clearly a FSC from a VFT law to an Arrhenius law. This crossover, is the signature of a FS dynamic transition predicted by Ito *et al* [19], and now extends into finite pressures. The transition temperature, T_L, as the crossing point of the VFT law and Arrhenius law, is calculated by $1/T_L = 1/T_0 - (Dk_B)/E_A$. However, in Fig. 7, the cusp-like transition becomes rounded off and there is no clear-cut way of defining the FSC temperature. Note that while we have done more measurements at high temperatures at 2000 bar pressure, shown in Fig. 7B, there is still a hint of fragile behavior at high enough temperature.

To determine the state of water before and after FSC, HRMECS measurements of INS were performed on 55 wt % water confined in MCM-41-S with 18 Å pore size. Fig. 8 shows the observed vibrational density of states (DOS) of confined water at different temperatures as compared with those of ice I*h*. It should be noted that $G(E)$ of ice (solid line) is characterized by a much steeper leaning edge compared to those of supercooled water in the temperature range from 210 K to 240 K. The broader $G(E)$ of supercooled water confined in MCM-41-S with pore diameter of 18 Å is seen to be more characteristic of a liquid state. From the behavior of the low-energy cut-off of the librational band around 50 meV, it is obvious that the state of confined water (its hydrogen bond network) is different at temperatures above and below 225 K. The difference between the average spectra above and below 225 K is shown to have a clear peak at around 50 meV (dash-dot-dot line). It is obvious from the figure that the confined water does not transform into ice at all these temperatures.

3.1.4 Discussion: the Liquid-Liquid Coexistence Line and the Associated Widom Line

According to the liquid-liquid phase transition hypothesis [50], to explain the anomalies of thermodynamic and transport properties of supercooled water, one postulates the existence of a first order phase transition line between two phases of liquid water: a low-density liquid (LDL) and a high-density liquid (HDL). This line is called Liquid-Liquid (L-L) coexistence line and terminates at a L-L critical point. It is to be noted that if the state point is on the L-L coexistence line, one has a two phase liquid consisting of a mixture of HDL and LDL, just as the gas and liquid phases are coexisting on the liquid-gas coexistence line (refer to the p - ρ diagram of superheated water, Fig. 2.2 of Ref. [51]). The L-L coexistence line extends into the one-phase region after terminating at the critical point [52]. This extended line, not being real, is the so-called Widom line or the critical isochore. The Widom line is defined as a straight line in the Pressure-Temperature (P-T) plane, starting from the critical point C^* (P_C, T_C) and extending into the one-phase region, with the same slope as that of the L-L coexistence line at (P_C, T_C). Even though this line is an imaginary line, experiments of superheated water show that many thermodynamic quantities and transport coefficients, such as the isothermal compressibility, thermal-expansion coefficient, isobaric specific heat capacity, isochoric specific heat capacity, speed of sound, thermal conductivity, shear viscosity and thermal diffusivity [51], show a peak when crossing the Widom line at a constant pressure.

Summarizing all the experimental results of fully hydrated MCM-41-S-14 under pressure, we show in a P-T plane, in Fig. 9 [56], the observed pressure dependence of T_L and its estimated continuation, denoted by a dash line, in the pressure region where no clear-cut FSC is observed. One should note that the T_L line has a negative slope, parallel to TMD line, indicating a lower density liquid on the lower temperature side. This T_L line also approximately tracks the T_H line, and terminates in the upper end when intersecting the T_H line at 1600 bar and 200 K, at which point the character of the dynamic transition changes. We shall discuss the significance of this point next.

Since T_L determined experimentally is a dynamic crossover temperature, it is natural to question whether the system is in a liquid state on both sides of the T_L, and if so, what would the nature of the high-temperature and low-temperature liquids be? Sastry and Angell have recently shown by a MD simulation that at a temperature $T \approx 1060$ K (at zero pressure), below the freezing point 1685 K, the supercooled liquid silicon undergoes a first-order liquid-liquid phase transition, from a fragile, dense liquid to a strong, low-density liquid with nearly tetrahedral local coordination [57]. Prompted by this finding, we may like to relate, in some way, our observed T_L line to the L-L transition line, predicted by MD simulations of water [58] and speculating on the possible location of the low-temperature critical point.

According to INS experiments, water remains in disordered liquid state both above and below the FSC at ambient pressure (Fig. 8). Furthermore, our analysis of the FSC for the case of ambient pressure indicates that the activation energy barrier for initiating the local structural relaxation is $E_A = 4.89$ Kcal/mol for the low-temperature strong liquid. Yet, previous INS experiments of stretch vibrational band of water [59] indicate that the effective activation energy of breaking a hydrogen bond at 258 K (high-temperature fragile liquid) is 3.2 Kcal/mol. Therefore, it is reasonable to conclude that the high-temperature liquid corresponds to the high-density liquid (HDL) where the locally tetrahedrally coordinated hydrogen bond network is not fully developed, while the low-temperature liquid corresponds

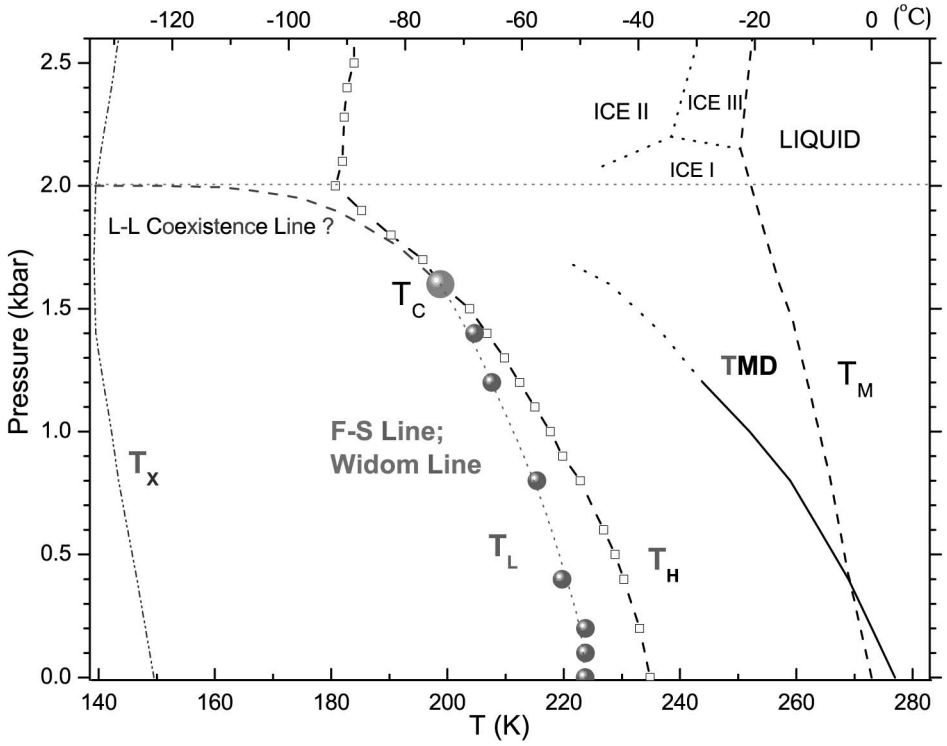

Fig. 9. The pressure dependence of the measured FS dynamic crossover temperature, T_L, plotted in the *P-T* plane (solid circles). Also shown are the homogeneous nucleation temperature line, denoted as T_H [53], crystallization temperatures of amorphous solid water, denoted as T_X [54] and the temperature of maximum density line, denoted as TMD [55], taken from known phase diagram of bulk water.

to the low-density liquid (LDL) where the more open, locally ice-like hydrogen bond network is fully developed [60].

It is appropriate now to address the possible location of the second critical point [58]. Above the critical temperature T_C and below the critical pressure p_C, we expect to find a one-phase liquid with a density ρ, which is constrained to satisfy an equation of state: $\rho = f(p,T)$. If an experiment is done by varying temperature T at a constant pres-sure $p < p_C$, ρ will change from a high-density value (corresponding to HDL) at sufficiently high temperature to a low-density value (corresponding to LDL) at sufficiently low temperature. Since the fragile behavior is associated with HDL and the strong behavior with LDL, we should expect to see a clear FSC as we lower the temperature at this constant p. Therefore, the cusp-like FSC we observed should then occur when we cross the so-called Widom line in the one-phase region [51]. On the other hand, if the experiment is performed in a pressure range $p > p_C$, corresponding to the two-phase region and crossing the L-L coexistence line, the system will be consisting of mixture of different proportions of HDL and LDL as one varies T. In this latter case, $\langle \tau_T \rangle$ vs. $1/T$ plot will not show a clear-cut FSC (the transition will be washed out) because the system is in a mixed state. The above picture would then explain the dynamical behavior we showed in Figs. 6 and 7. In Figs. 6 and 7, a clear FSC is observed up to 1400 bar and beyond 1600 bar the crossover is rounded off. From this observation, the reasonable location of the L-L critical point is estimated to be at $P_C = 1500 \pm 100$ bar and $T_C = 200 \pm 10$ K, shown by a big round point in Fig. 9.

Additionally, in a recent MD simulation using TIP5P, ST2 and Jagla Model Potential of Xu [61], a small peak was found in the specific heat C_P when crossing the Widom line at a constant p. Meanwhile, Maruyama *et al.* conducted an experiment on adiabatic calorimetry of water confined within nano-pores of silica gel [62]. It was found that water within 30 Å pores was well prevented from crystallization, and also showed a small C_P peak at 227 K at ambient pressure. This experimental result further supports that the FSC we observed at 225 K at ambient pressure is caused by the crossing of the Widom line in the one-phase

region above the critical point [61].

3.1.5 Conclusion on Observation of FSC in Supercooled Water Confined in MCM-41-S

In conclusion, we make a detail account of our QENS studies of the dynamics of supercooled water confined in nanoporous silica materials, MCM-41-S with different pore sizes and under pressure.

QENS data were analyzed by using RCM model previously developed by us. Four quantities are extracted from the analysis: they are p, τ_0, β and γ. In particular, we discuss the temperature dependence of $\langle \tau_T \rangle = \frac{\tau_0}{\beta}\Gamma(1/\beta)$ at ambient pressure and noted that the rate of dynamic slowing down changes abruptly at the temperature around 225 K, signaling the onset of an avoided structural arrest transition of a high density water into a low density water. This FSC, then, has been determined for $\langle \tau_T \rangle$ at about 225 K.

Moreover, we study the slow dynamics of supercooled confined water under various applied pressures using HFBS and DCS. We observe clear evidence of a cusp-like FSC at pressures lower than 1600 bar. We show, in this section, that the crossover temperature decreases steadily with an increasing pressure, until it intersects the homogenous nucleation temperature line of bulk water at a pressure of 1600 bar. Above this pressure, it is no longer possible to discern the characteristic feature of the FSC.

This paper elaborates the detailed analysis of experimental data, and in that process, it elucidates the new finding that the FSC is the result of crossing the Widom line at a constant pressure. We then estimate the location of the end point of the Widom line which should be the much anticipated second critical point of water. It is our future task to search for the locus of the L-L coexistence line and establish experimentally the existence of the L-L phase transition phenomena in water.

3.2 A new Discovery of a Dynamic Crossover Phenomenon in Protein Hydration Water

At low temperatures proteins exist in a glassy state [63, 64], a state which has no conformational flexibility and shows no biological functions. In a hydrated protein, at and above 220 K, this flexibility is restored and the protein is able to sample more conformational sub-states, thus becomes biologically functional. This 'dynamical' transition of protein is believed to be triggered by its strong coupling with the hydration water, which also shows a similar dynamic transition. Here we demonstrate experimentally that this sudden switch in dynamic behavior of the hydration water on lysozyme occurs precisely at 220 K and can be described as a FSC [49,56]. At FSC, the structure of hydration water makes a transition from predominantly high-density (more fluid state) to low-density (less fluid state) forms derived from existence of the second critical point at an elevated pressure [56,61].

Without water, a biological system would not function. Dehydrated enzymes are not active, but a single layer of water surrounding them restores their activity. It has been shown that the enzymatic activity of proteins depends crucially on the presence of at least a minimum amount of solvent water [65,66]. It is believed that about 0.3 g of water per g of protein is sufficient to cover most of the protein surface with one single layer of water molecules and to fully activate the protein functionality. Thus, biological functions [67], such as enzyme catalysis, can only be understood with a precise knowledge of the behavior of this single layer of water and how that water affects conformation and dynamics of the protein. The knowledge of the structure and dynamics of water molecules in the so-called hydration layer surrounding proteins is, therefore, of utmost relevance to the understanding of the protein functionality. It is well documented that at low temperatures proteins exist in a glassy state [68,69], which is a solid-like structure without conformational flexibility. As the temperature is increased, the atomic motional amplitude within the protein increases linearly initially, as in a harmonic solid. In hydrated proteins, at approximately 220 K, the rate of the amplitude increase suddenly becomes enhanced, signaling the onset of additional anharmonic and liquid-like motion [63,64,70]. This 'dynamical' transition of proteins is believed to be triggered by their strong coupling with the hydration water through the hydrogen bonding between them. The reasoning is derived from the finding that the protein hydration water shows some kind of dynamic transition at the similar temperature [71,72]. We demonstrate in this section, using QENS spectroscopy, that this dynamic transition of hydration water on lysozyme protein is in fact the Fragile-to-Strong dynamic crossover (FSC) at 220 K, similar to that recently observed in confined water in cylindrical nanopores of silica materials [see section III.A and refs. 49 and 56]. Computer simulations on both bulk water [61] and protein hydration water around lysozyme [73] have led to the interpretation of the FSC as arising from crossing the locus of maximum in the correlation length ('Widom line') which emanates from a critical point into the one-phase region; if this interpretation is correct, then our experiments provide evidence supporting the existence of a liquid-liquid critical point in protein hydration water, which previously has been proposed only for bulk water [58].

Water molecules in a protein solution may be classified into three categories: (i) the bound internal water, (ii) the surface water, i.e., the water molecules that interact with the protein surface strongly, and (iii) the bulk water. The bound internal water molecules, which occupy internal cavities and deep clefts, are extensively involved in the protein-solvent H-bonding, and play a structural role in the folded protein itself. The surface water, or usually called the hydration water, is the first layer of water that interacts with the solvent-exposed protein atoms of different chemical character, feels the topology and roughness of the

protein surface, and exhibits the slow dynamics. Finally, water, which is not in direct contact with the protein surface but continuously exchanges with the surface water, has properties approaching that of bulk water. In this section, we deal with dynamics of the hydration water in a powder of the globular protein lysozyme. This hydration water is believed to have an important role in controlling the biofunctionality of the protein.

The biochemical activity of proteins also depends on the level of hydration. In lysozyme, enzymatic activity remains very low up to a hydration level (h) of 0.2 (h is measured in g of water per g of dry protein) and then increases sharply with an increase in h from 0.2 to 0.5 [74]. Various experiments [75] and computer simulations [76] have demonstrated the strong influence of the hydration level on protein dynamics.

It has been found that many proteins exhibit a sharp slowing down of their functions (kinetic of biochemical reactions) at a temperature somewhere within the interval of T between 200 K and 250 K. An analysis of the mean-squared atomic displacement, $\langle x^2 \rangle$, by using Mössbauer [77], X-ray [64], and neutron scattering [78] spectroscopy, in hydrated proteins shows sharp changes around a certain sample temperature range: $\langle x^2 \rangle$ varies approximately linearly as a function of T at low T and then increases sharply above T between 200 K and 250 K. The sharp rise in $\langle x^2 \rangle$ was attributed to a certain dynamic transition in biopolymers at this temperature range. The coincidence of the characteristic temperatures, below which the biochemical activities slow down, and the on-set of the dynamic transition, suggests a direct relation between these two phenomena. It has also been demonstrated that the dynamic transition can be suppressed in dry biopolymers, or in biopolymers dissolved in trehalose [79]. It can also be shifted to higher temperatures, e.g. between 270 K and 280 K, for proteins dissolved in glycerol [80]. Thus the solvent plays a crucial role in the dynamic transition in biopolymers. This observation led to a suggestion by many authors that proteins are `slaves' to the solvent [81]. Despite many experimental studies, the nature of the dynamic transition in proteins remains unclear. Many authors interpret the dynamic transition as a kind of glass transition in a biopolymer [63,82]. Our experiments described below demonstrate that the origin of the characteristic temperature controlling

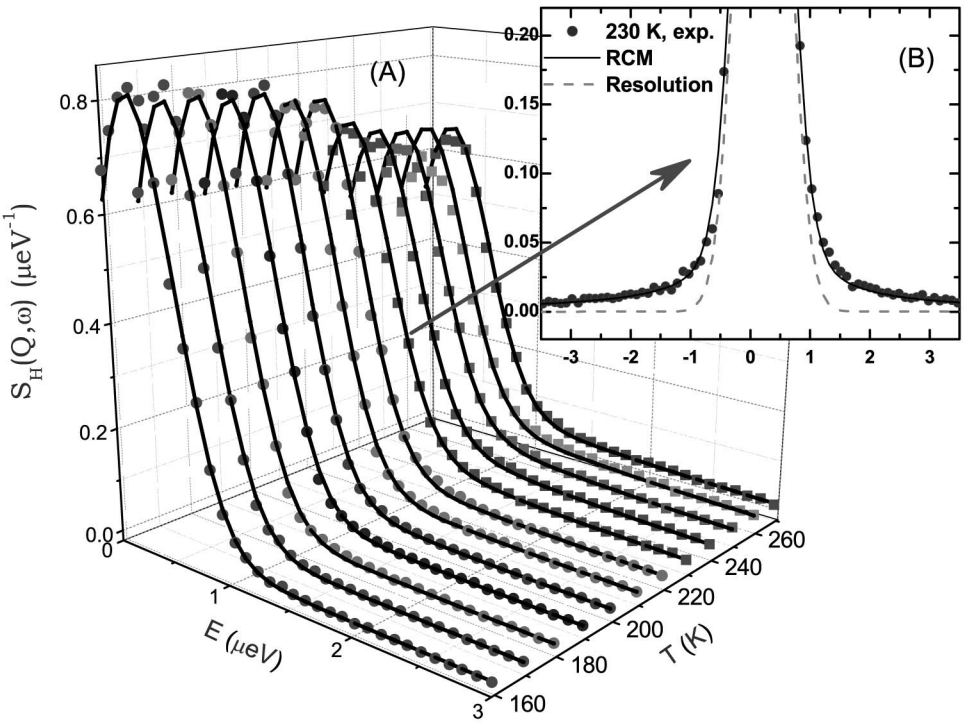

Fig. 10. Neutron spectra and their RCM analyses. Panel A displays measured QENS spectra (solid symbols) and their RCM analysis results (solid lines) at Q = 0.87 Å^{-1} and at a series of temperatures. Panel B singles out one particular spectrum at T = 230 K and contrasts it with the resolution function of the instrument for this Q value (dash line).

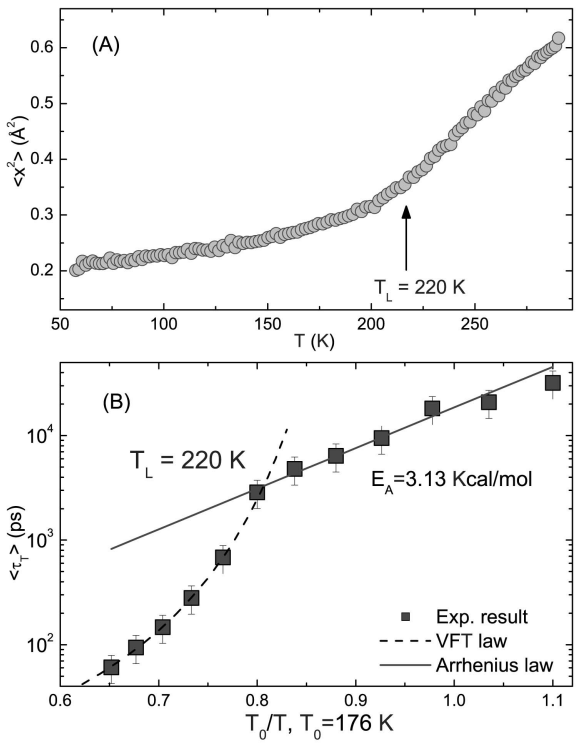

Fig. 11. Evidence for the dynamic transition. Panel A shows the temperature dependence of the mean-squared atomic displacement of the hydrogen atom at 2 nanosecond time scale measured by an elastic scan with resolution of 0.8 μeV. Panel B shows temperature dependence of the average translational relaxation times plotted in log($\langle \tau_T \rangle$) versus T_0/T, where T_0 is the ideal glass transition temperature. In this figure, there is a clear and abrupt transition from a VFT law at high temperatures to an Arrhenius law at low temperatures, with the fitted crossover temperature T_L = 220 K and the activation energy E_A = 3.13 Kcal/mol extracted from the Arrehenius part indicated in the figure.

both the activity of the protein and the transition in the behavior of $\langle x^2 \rangle$ is the FSC phenomenon in the hydration water, which shares the same crossover temperature with the protein.

Hen egg white lysozyme was used in this experiment. The dried protein powder was hydrated isopiestically at 5 °C by exposing it to water vapor in a closed chamber until h = 0.3 is reached. This hydration level was chosen to have almost a monolayer of water covering the protein surface [83]. A second sample was then prepared using D_2O in order to subtract out the incoherent signal from the protein hydrogen atoms. Both hydrated samples had the same water or heavy water/dry protein molar ratio. DSC analysis was performed in order to detect the absence of any feature that could be associated with the presence of bulk-like water.

High-resolution incoherent QENS spectroscopy method is used to determine the temperature dependence of the average translational relaxation time for the hydration water. In this experiment, we measured both an H_2O hydrated sample and a D_2O hydrated sample, and take the difference to obtain the signal contributed solely from hydration water. Because neutrons are predominantly scattered by an incoherent process from the hydrogen atoms in water (rather than by the coherent scattering process from the oxygen atoms), high-resolution QENS technique is an appropriate tool for the study of diffusional process of water molecules. Using the HFBS in NIST NCNR, we are able to measure the average translational relaxation time (α-relaxation time) from 60 picoseconds to 20 nanoseconds over the temperature range of 270 K to 180 K, spanning both below and above the FSC temperature. For the chosen experimental setup, the spectrometer has an energy resolution of 0.8 μeV and a dynamic range of $\pm$11 μeV [14], in order to be able to extract the broad range of relaxation times covering both the fragile and the strong regimes of the relaxation times from measured spectra.

Using high-resolution QENS method and the Relaxing-Cage Model (RCM, described in section 3.1) [31] for the analysis, we determine the temperature dependence of the average translational relaxation time, $\langle \tau_T \rangle$, for the hydration water. In the case of hydration water in lysozyme, we found the FSC temperature T_L = 220 K, which agrees well with the characteristic transition temperature in protein observed before [64]. Since the average relaxation time $\langle \tau_T \rangle$ is a measure of the mobility of a typical hydration water molecule, this result implies that the sudden change in the trend of mobility of water molecules at the crossover temperature triggers the so-called glass transition of protein molecules [63,76,82].

Fig. 10 shows the result of RCM analysis of the spectra taken at Q = 0.87 Å^{-1} for a series of temperatures ranging from 270 K to 160 K (panel A), and in particular at T = 230 K (panel B). In this figure, we display the instrument resolution function purposely for comparison with the measured spectrum. RCM, as one can see, reproduces the experimental spectral line shapes of hydration water quite well. The broadening of the experimental data over the resolution function leaves enough dynamic information to be extracted by RCM. This means that it requires a high-resolution backscattering instrument with an energy resolution of 0.8 μeV to adequately study the FSC phenomena in hydration water.

In Fig. 11, we first present (in panel A) the mean-squared atomic displacement $\langle x^2 \rangle$ (calculated from the translational Debye-Waller factor, $S_H(Q,E=0)=\exp[-Q^2\langle x^2 \rangle]$ of the hydrogen atoms versus T to indicate that there is a hint of a dynamic transition at a temperature between 200 K and 220 K. In panel B, we then present in an Arrhenius plot the temperature dependence of the average translational relaxation time, $\langle \tau_T \rangle$, for the hydrogen atom in a water molecule calculated by Eqs. (1), (8), (10), (11) and (12). The contribution from hydrogen atoms in the protein has

been subtracted out during the signal processing. It is seen that, in the temperature range 270-230 K, $\langle \tau_T \rangle$ obeys VFT law, a signature of fragile liquid, quite closely. But at T = 220 K it suddenly switches to an Arrhenius law, a signature of a strong liquid. So we have a clear evidence of FSC in a cusp form. The T_0 for the fragile liquid turns out to be 176 K, and the activation energy for the strong liquid, E_A = 3.13 Kcal/mol [84].

Recently, E. Mamontov observed a similar dynamic crossover in the surface water on cerium oxide powder sample [85]. The surface of cerium oxide is hydroxylated. The coverage of water is about 2 layers and the crossover temperature is said to be at 215 K. The observed slow dynamics is attributed to the effect on the translational mobility of the water molecules in contact with the surface hydroxyl groups. Thus, our observation of the FSC in hydration water of protein may be a universal phenomenon for surface water.

It should be noted that the FSC in confined supercooled water is attributed to the crossing of the so-called Widom line in the Pressure-Temperature (phase) plane in a recent MD simulation work on bulk water [61] and protein hydration water at ambient pressure [73]. The Widom line is originated from the existence of the second critical point of water and is the extension of the liquid-liquid coexistence line into the one phase region. Therefore, our observation of the FSC at ambient pressure implies that there may be a liquid-liquid phase transition line in the protein hydration water at elevated pressures. This dynamic crossover, when crossing the Widom line, causes the layer of the water surrounding a protein to change from the 'more fluid' high-density liquid form (which induces the protein to adopt more flexible conformational sub-states) to the 'less fluid' low-density liquid structure (which induces the protein to adopt more rigid conformational sub-states).

In summary, an investigation of the average translational relaxation time, or the α-relaxation time, of protein hydration water as a function of temperature reveals a hitherto un-noticed Fragile-to-Strong dynamic crossover at 220 K, close to the universal dynamic transition temperature documented for proteins in literature. This fact implies that the sudden transition of the water mobility on the surface of a protein at the FSC triggers the so-called glass transition, which is known to have a profound consequence on biological function of the protein itself.

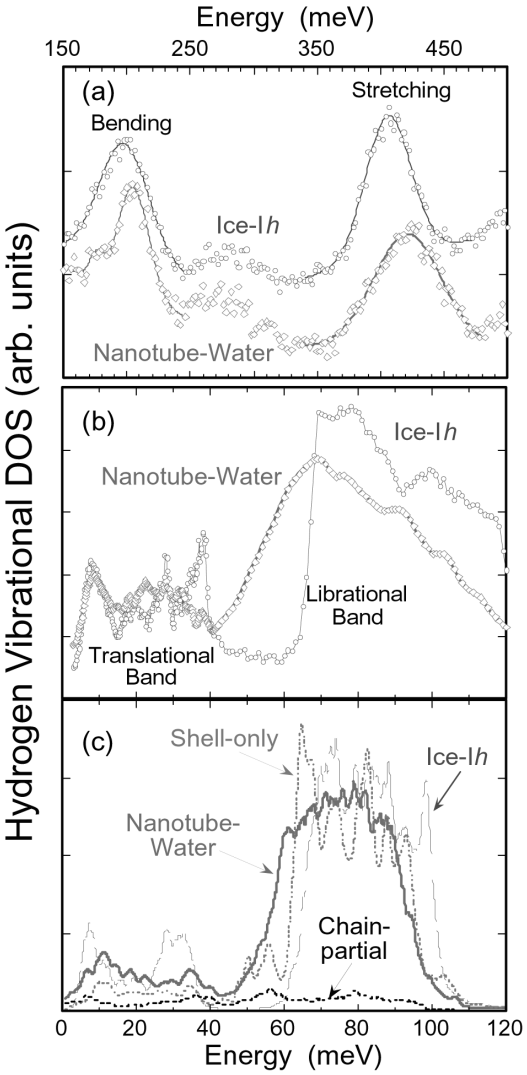

Fig. 12. The observed neutron-weighted hydrogen vibrational DOS of nanotube-water and ice-Ih at 9K: (a) the bending and stretching band and (b) the translational and librational band. (c) The corresponding simulated DOS for nanotube-water and ice-Ih. Chain-partial is the partial DOS from the chain contribution and shell-only is the DOS from a separated MD simulation for only a shell of water in SWNT.

3.3 Water Confined in Single-wall Open-ended Carbon Nanotubes

The recently discovered carbon nanotubes and related nanocarbon materials exhibit a variety of outstanding properties such as high mechanical strength, thermal conductivity and heat resistant in the absence of oxygen, tunable electrical characteristics, controlled porous structure and large surface area, etc. This, in conjunction with the natural abundance, stability, environmental inertness, light weight and low cost of carbon, have motivated intense research on the applications of carbon nanotubes, as stand-alone devices or key components in composites, in nanotechnology and engineering [86,87]. Water encapsulated in carbon nanotubes represents an interesting scenario contrasting to water in oxide-based porous media or hydrated water in proteins. First, unlike the strong interfacial interaction between water molecules and the oxides or proteins, the nanotube walls are hydrophobic and interactions between the water molecules and the carbon atoms are weak. Secondly, the quasi-one-dimensional geometry with a uniform sp^2-bonded structure of carbon nanotubes differs

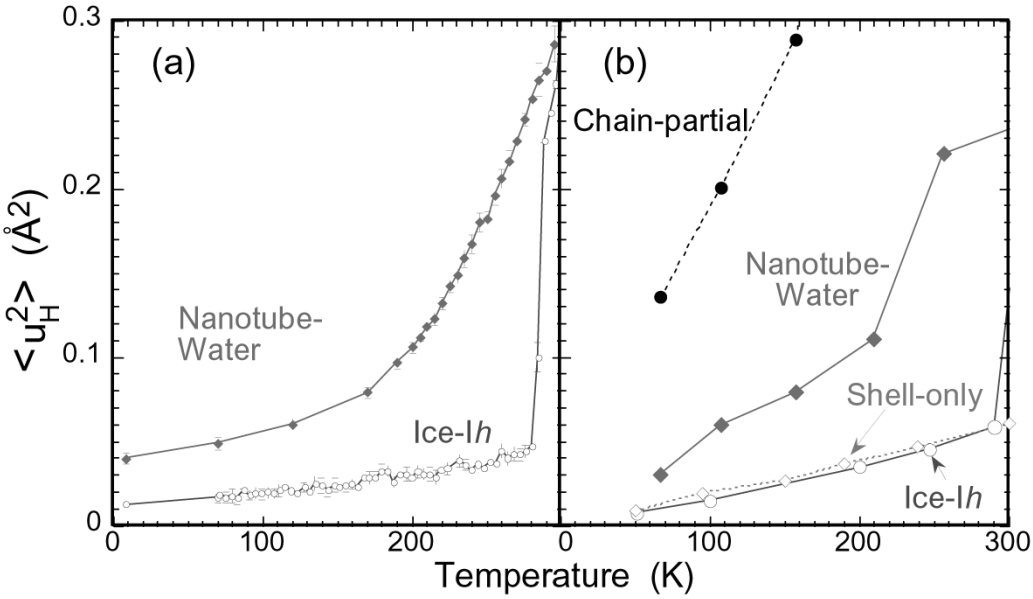

Fig. 13. The observed (a) and simulated (b) hydrogen mean-square displacements for nanotube-water and ice-I*h*. The simulated for hydrogen atoms in the chain of nanotube-water and in the shell-only configuration are also given in b.

from the inter-connected framework of internal pores in silica or the complex curvature of a protein surface. Finally, the highly anisotropic force fields with respect to the directions parallel and perpendicular to the nanotube axis are unique. On the other hand, in some transmembrane water channels, such as aquaporins [88] commonly found in bacteria, plants and mammals, the pathways are formed by parallel-packed alpha helices across the membrane with hydrophobic interfaces, somewhat similar to the channels inside carbon nanotubes. Therefore, water in carbon nanotubes provides a simplified model for studying water/proton transport across biological membranes.

The procedure of introducing water into highly purified, well-characterized open-ended single-walled carbon nanotubes (SWNT) (diameter of 14 Å) with the end product of water confined only in the interior of the SWNT, to which we referred as nanotube-water, was described elsewhere [89]. The confinement was verified experimentally by ensuring the neutron diffraction data from mixed H_2O-D_2O nanotube-water samples agreeable with all the corresponding calculated intensities for water *inside* the SWNT only. The optimal H_2O/SWNT mass ratio is about 11%.

Insights in the detailed structure and atomic dynamics of nanotube-water were obtained from a combined INS and molecular-dynamics (MD) study. Fig. 12a shows the INS spectrum of the intramolecular O-H stretch and H-O-H bending modes. These modes, located at respectively 406 and 199 meV in ice-I*h*, are noticeably shifted to higher energies in nanotube-water, i.e. 422 and 205 meV. These blue shifts imply a shorter intramolecular O-H bond length in nanotube-water compared to that in bulk ice-I*h*, and from the phenomenological model of Klug and Whalley [90], we estimate an O-O distance between nanotube-water molecules to be 2.916 Å, more than that (2.76 Å) for ice-I*h*. These data are shown in Fig. 12b, where the ice-I*h* and nanotube-water spectra are compared. In this energy region, the well-defined band of translational modes below 40 meV and a librational band rising up sharply above 64 meV are characteristic of bulk ice-I*h* [91]. The intermolecular vibrations of nanotube-water, see Fig. 12b, shift overall towards lower energies, i.e., with the librational band rising slowly at 40 meV (the midpoint of onset is at 55 meV), and its translational modes softened to form a broadened band with much less weight at 35-40 meV as compared to those (well-defined translational modes below 40 meV and a librational band rising up sharply above 64 meV) characteristic of bulk ice-I*h*. These red (blue) shifts of the intermolecular (intramolecular) modes support the weakening of the hydrogen-bonded water network in nanotube-water.

Hydrogen mean-square displacement $\langle u^2_H \rangle$ is a good measure of the hydrogen vibration amplitude provided that atomic migration from one molecule to another and molecular diffusion do not happen; otherwise the hydrogen motion is better quantified by the analysis of the quasielastic scattered intensity. The $\langle u^2_H \rangle$ for ice-I*h*, as shown in Fig. 13a increases slowly at a rate almost constant with temperature up to the melting temperature of 273 K, reflecting a temperature dependence for which hydrogen vibrations are approximated by harmonic oscillations. The abrupt jump of $\langle u^2_H \rangle$ at 273 K arises from melting of ice-I*h*. The

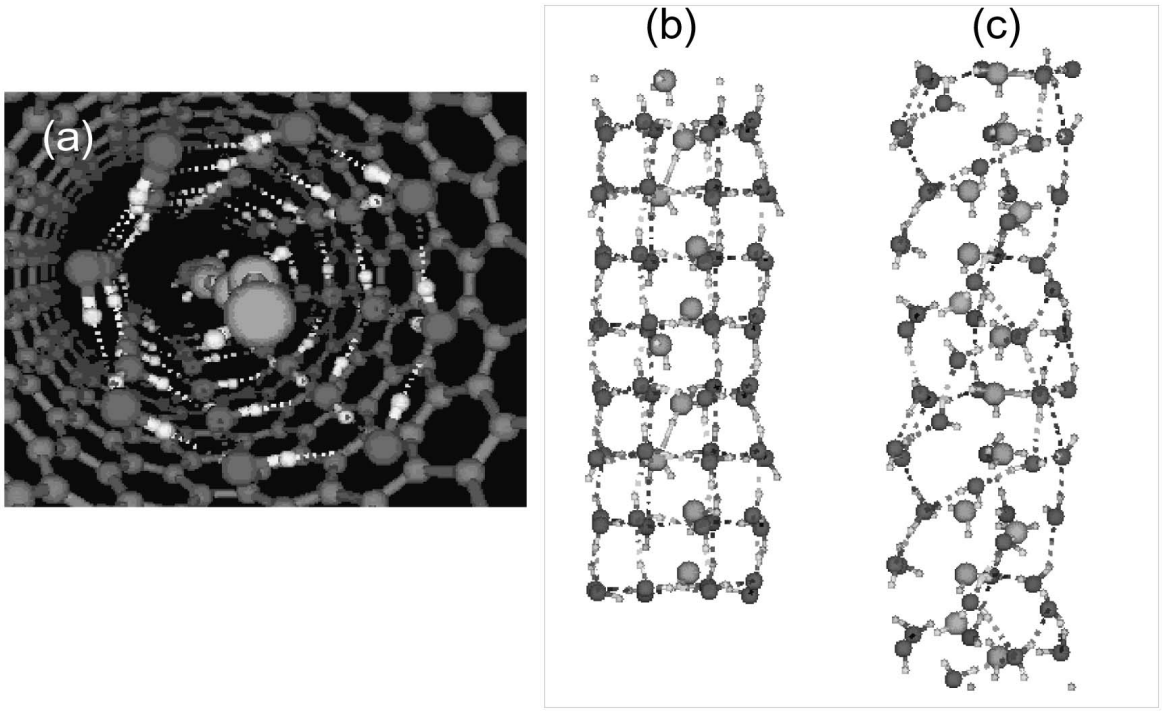

Fig. 14. MD simulation snapshots: The shell + chain structure of nanotube-water below 210 K (a and b) and the disappearance of the shell + chain structure at temperatures above 210 K (c).

$\langle u^2_H \rangle$ of nanotube-water differs drastically from that of ice-I*h*. The values are much higher, about four times as large at 8 K, increasing nearly linearly with rising temperature until about 200 K then escalating much faster at higher temperatures. The curve of $\langle u^2_H \rangle$ is smooth but it displays a change of the slope around 210 $\pm$ 10 K. This, in conjunction with the appearance of a quasielastic scattering component above ~210 K, suggest a sluggish change of the nature of hydrogen dynamics in nanotube-water from predominately local vibrations to diffusive motion. MD simulations of nanotube-water were performed on a rigid (10,10) SWNT of 13.8 Å in diameter and 40 Å in length enclosing 126 water molecules [89]. The water-carbon and water-water interactions were represented by a Lennard-Jones and the TTM2-F polarizable flexible water model, respectively, both of which were validated separately by experiments [92,93]. The TTM2-F polarizable flexible water model, using smeared charges and dipoles to model short-range electrostatics, was able to accurately account for the high-level electronic structure data of water clusters and to reproduce the bulk behavior of ice and ambient liquid water. For comparison MD simulations of ice-I*h* and liquid water were carried out using the TTM2-F model. An Ewald sum was used to incorporate the long-range Coulomb interactions and periodic boundary conditions were applied to take care of surface effects.

Achieving ergodicity is one of the most challenging problems in computational statistical mechanics. Conventional single-trajectory molecular dynamics tends to get stuck in local regions of phase-space and cannot easily locate low-lying minima such as crystalline structures. To circumvent this problem we employed a 'parallel tempering' molecular dynamics (PTMD) algorithm [94] which calculates simultaneously multiple trajectories, each assigned to a different temperature. Occasionally swapping temperatures between neighboring trajectories is administered effectively allowing the system to heat up temporarily to escape over intermediate local barriers and then to cool down for annealing in the vicinity of low energy regions of the potential energy surface. This technique proved to be essential to assess structural variations and dynamic processes over a wide range of temperatures and pressures for comparison with experimental results.

The MD simulation predicted a shell + chain structure of nanotube-water at temperature below ~210 K, as shown in Fig. 14a. The shell consists of a fourfold-coordinated 'square-ice' sheet rolled into a hollow cylinder parallel the SWNT long axis in a tube-in-tube configuration. A gap of ~3 Å is maintained between the nanotube wall and the shell as a direct consequence of the hydrophobic interaction between the water molecules and carbon atoms. The chain is formed by a single file of water molecules along the

centerline of the shell with an average coordination number of 1.86. The shell + chain configuration, as shown in Fig. 14a, depicts only a time-average picture. In reality, the atoms undergo vibrations depending on the local-field environment, which, in the case of water, is critically influenced by the hydrogen-bond energetics. The weakened hydrogen bonds in nanotube-water, as revealed in the INS spectra and the observed $\langle u_H^2 \rangle$, are elucidated by the MD simulations through the unique shell + chain structure. Simulations show that the hydrogen bonds in nanotube-water are in general weaker than those in ice-I*h*. A shell-only configuration, as suggested by Koga *et al*. [95] in their simulations, is not sufficient to explain the INS and $\langle u_H^2 \rangle$ data, as shown in Fig. 12b and 13b. Only the shell + chain model can account for the softening of the librational band and the broadening of the translational modes. Specifically, the hydrogen bonds connecting the chain molecules or molecules between the shell and the chain are very pliable or even momentarily broken or reform. Such enhanced fluctuations in the hydrogen motion of the chain molecules give rise to significant contributions to the very large $\langle u_H^2 \rangle$ even at low temperatures, see Fig. 13b.

As temperature rises, dynamic fluctuations of hydrogen bonds between the square-ice shell network and the chain increase. Above ~210 K the shell-chain structure vanishes and nanotube-water behaves, to a certain extent, like supercooled liquid water that supports long-range molecular diffusion (see Fig. 14b). What are the similarities and differences between water confined in SWNT and water in nanoporous silica (e.g. MCM-41-S) or proteins? Thus far INS experiments have not yet been carried out to the extent affording full comparison with the water in MCM-41-S. However, initial results are encouraging. Our preliminary INS study shows a spectral change of the hydrogen vibrational DOS in nanotube-water qualitatively similar to that of water in MCM-41-S as the systems enter the supercooled state from low temperatures. We also performed QENS measurements of the relaxation processes in nanotube-water. The initial results show a crossover at 218 K from a VFT law to an Arrhenius behavior typical of a fragile-to-strong liquid transition in confined water, compared to 224 K for water in MCM-41-S [96]. The activation energy of 5.4 kJ/mol, obtained from the Arrhenius behavior at low temperature, is 3.8 times smaller than that for water in MCM-41-S. Clearly, more neutron and MD investigations over extended temperature and pressure regimes are needed to clarify the nature of the transition in nanotube-water.

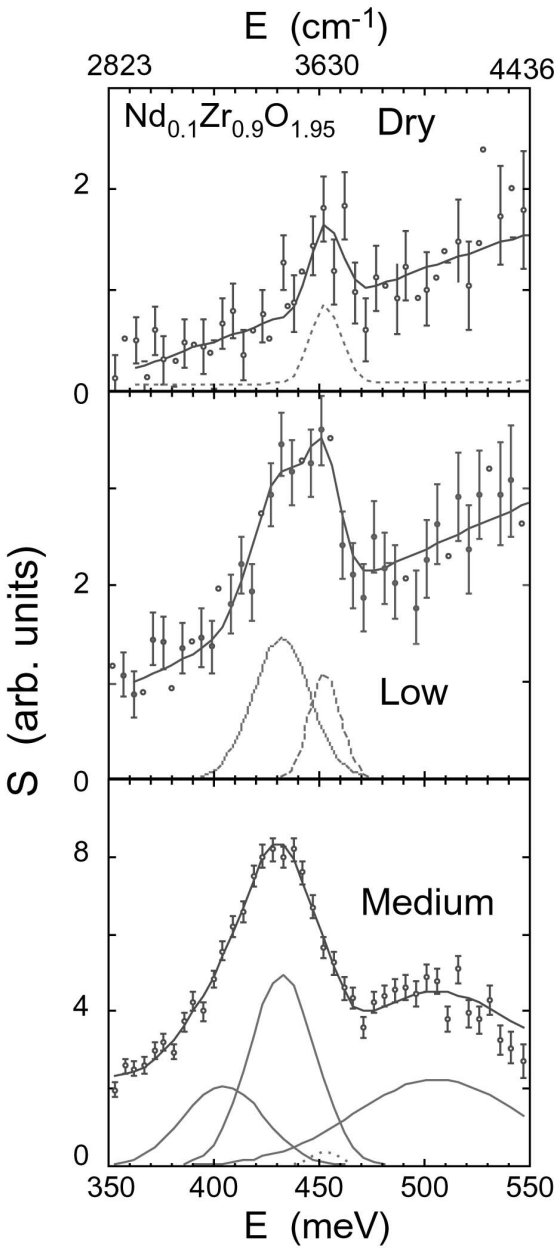

Fig. 15. The O-H stretch vibrational band of chemisorbed hydroxyl groups on dry $Nd_{0.1}Zr_{0.9}O_{1.95}$ nanoparticles (a) and physisorbed low-water-content (b) and medium-water-content (c) samples of $Nd_{0.1}Zr_{0.9}O_{1.95}$ nanoparticles. The lines through the data are fits of a linear background and one or more Gaussian functions (see text). For Clarity, error bars are given for selected data points for the dry and low-water-content sample.

3.4 Water and Hydroxyl Species in Nanostructured Minerals

Water is present in hundreds of minerals as inherent structural units, hydroxyl or complex cations, and weakly- or non-bonding entities. Therefore, its roles in the natural environment and indirectly in man-made substances derived from minerals are enormous. Furthermore, implementation of nanostructure in the host mineral adds a new dimension to tailoring the structure-function relationship, which is important to technological applications. For example, zirco-

nias as bulk ceramics are widely used in industry as refractory components, matrix medium for nuclear fuel, cutting tools, etc., but high-surface-area nanostructured zirconias are applicable as catalytic supports [97], sensors [98] and an agent for radiolysis of liquid water [99]. The latter applications underscore the importance of understanding chemi- and physisorbed water on zirconia nanoparticles.

3.4.1 Dynamics of Adsorbed Water on Zirconia Nanoparticles

Fig. 15 shows the INS spectra over the region of O-H stretch vibrations for water adsorbed on a nanostructured $Nd_{0.1}Zr_{0.9}O_{1.95}$ powder (with a surface area of ~73 m^2/g estimated by the Brunauer-Emmett-Teller gas-adsorption method) [100]. The partial substitution of Zr by Nd yields a solid solution featuring a mixed-phase of cubic and tetragonal crystal structure and oxygen vacancies in the lattice in instead of the monoclinic phase of pure ZrO_2 at room temperature and enhances thermal stability at high temperatures in a moist atmosphere. These properties are important to catalytic applications such as being a support component for a three-way catalytic converter for automobile emission control. The dry powder contains only chemisorbed hydroxyl groups on the surfaces of the nanoparticles. The low- and medium-water-content samples refer to statistically 0.747 and 2.54 layers of physisorbed water on the surface, respectively. Each observed spectrum (symbols) was fitted to a sum of a linear background and one or more Gaussian functions (line). In the dry sample the O-H stretch band of the surface hydroxyl groups centers at 453 meV (3654 cm^{-1}) with a width of about 17 meV, which is comparable to the instrumental resolution. An additional broad component at about 432 meV appears in the low-water-content sample, which arises from O-H stretch vibrations of physisorbed water molecules connected with hydrogen bonds. In the medium-water-content sample that contains multiple layers or clusters of hydrogen-bonded water, the OH-stretch vibrational band broadens and shifts to lower energies, which is accounted for by another Gaussian at ~405 meV. In addition, a H-O-H bending mode and a libration mode at 200 and 80 meV (not shown) resembling those in bulk water appear, and the very broad component center around 510 meV corresponds to a combination mode of the libration and stretch bands. Similar features were also observed in pure nanostructured ZrO_2 powders containing absorbed water.

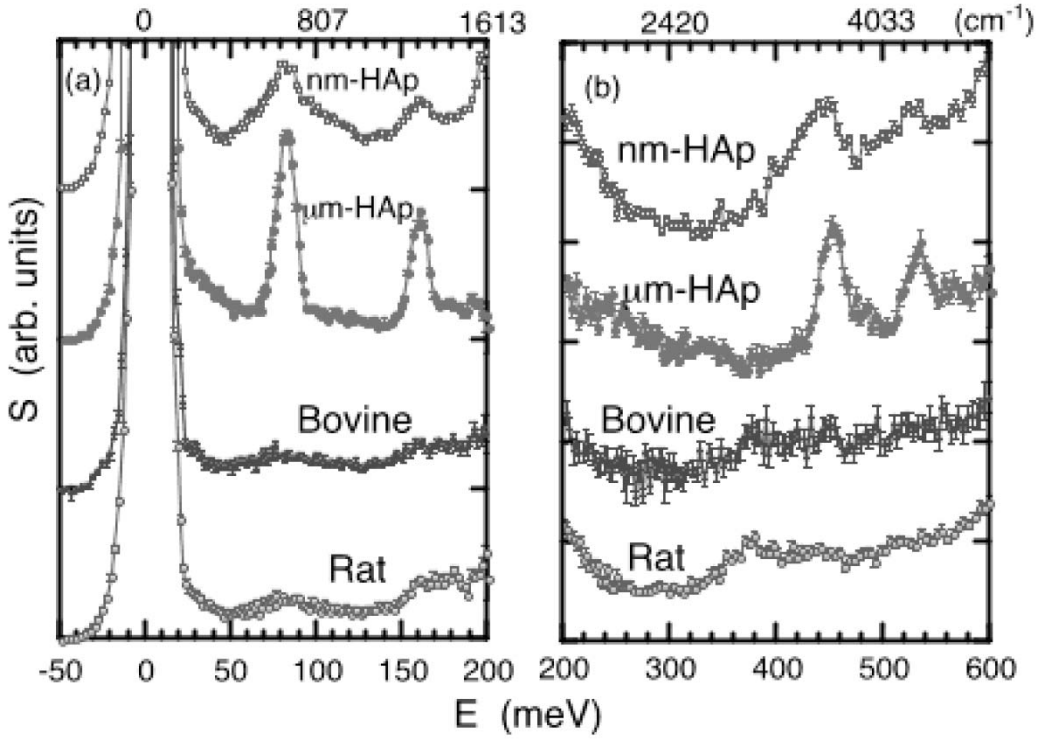

Fig. 16. The low-energy (a) and high-energy (b) portion of the observed neutron spectra of micron- and nanometer-size HAp crystalline powders, and the bovine and rat bone crystals at 10 K. For clarity, the HAp and bovine bone spectra are shifted vertically by a constant interval.

The progressive softening of the H-O stretch frequency in parallel to the build-up of hydrogen-bonded network of water from the immediate interface to the outer hydrated layers to the bulk-like liquid has direct consequence to the slow-down dynamics of water molecules near the surface. In recent QENS studies of surface water on ZrO_2, a translational dynamics slowed down by 1 and 2 orders of magnitude was observed in the outer hydration layer and the immediate interfacial layer, respectively, as compared to that of bulk water [101,102]. Furthermore, the very slow motion of the immediate interfacial water can be described by a relaxation function characterized by a stretched exponential, indicative of complex diffusive processes of distinct relaxation times. The outer hydration layers, on the other hand, exhibit separate Arrhenius-type rotational and translational diffusion motion, both considerably slower than the corresponding one in bulk water. This dichotomy of lower density-slower dynamics of an interfacial water layer and higher density-faster dynamics of bulk water away from the substrate arises from the hydrophilic nature common to oxide surfaces and was corroborated by computer simulations [103].

3.4.2 Hydroxyl Ions in Nanostructured Bone Apatite Crystals

Bone is a nanocomposite containing principally collagen and mineral apatite. As compared to synthetic hydroxyapatite (HAp with chemical formula $Ca_{10}(PO_4)_6(OH)_2$) which normally has micrometer-size crystallites, bone apatite consists of platelet-shaped nanocrystals exhibiting rough surfaces, calcium deficiency, and possibly ion substitutions by CO_3 and HPO_4 groups [104]. The crystal chemistry of bone apatite, such as the role of the bioactive ions presumably located on the surface or on modified mobile lattice sites, is important to biological functions which include bone remodelling and homeostasis. Due to the nanoscale dimensions and poor crystallinity, the content and location of the hydroxyl ions in bone apatite have not been firmly established despite numerous diffraction and spectroscopic studies and the subject is still controversial today. INS measurements find, as shown in Fig. 16, no sharp excitations characteristic of the librational mode and stretch vibrations of OH ions around 80 and 450 meV (645 and 3630 cm^{-1}), respectively, in the bovine and rat bone apatites, whereas such salient features are clearly seen in micron- and nanometer-size crystals of pure hydroxyapatite powders [105]. Thus the data provide additional definitive evidence for the lack of well-localized OH^- ions in the crystals of bone apatite. Weak features at 160-180 and 376 meV, which are observed in the apatite crystals of rat bone and possibly also in adult mature bovine bone, but not in the synthetic hydroxyapatite, are assigned to the deformation and stretch modes of OH ions belonging to HPO_4^- species.

Water and its variant species in minerals, incorporated naturally or synthetically, often play an important role in controlling the mechanical, chemical and thermodynamic properties and functionality. Excess water in boehmite, γ-AlOOH, produced by hydrolysis methods, yields a mass-fractal-like aggregate of nanoparticles of pseudoboehmite [106]. Water stored in the hydrogarnets, e.g., $Sr_3Al_2(O_4H_4)_3$, may be released in the Earth and acts as a catalyst for certain type of geochemical reactions [107]. The question of whether oxonium ions (H_3O^+) are present in H_3O-anluite, $H_3OAl_{2.87}(SO_4)_2(OH)_{5.64}(H_2O)_{0.39}$, remains unanswered today [108]. Protonated λ-MnO_2 or $H_xMn_2O_{4-y}$ nanopowders is used as a means to scavenge lithium from seawater [109]. These examples and other similar problems can be benefited by neutron spectroscopic investigations.

4. SUMMARY

In this article we introduce the basic principles and practice of incoherent neutron scattering spectroscopy. Specifically, the scattering functions of elastic, quasielastic and inelastic processes from a many-body system of incoherent scatterers and measurements of these scattering functions using a suite of state-of-the-art spectrometers at reactor- and accelerator-based neutron sources are described. We apply this method to the studies of water confined in nanometer-scale porous media – MCM-41-S silica materials, proteins, and carbon nanotubes– and incorporated in nanostructured minerals – zirconia and bone apatite. Through combined neutron-scattering and molecular dynamics simulations or theoretical-modeling investigations, we demonstrate the outstanding capability of obtaining very detailed information regarding the structure and dynamics of water molecules in a complex environment. We have chosen these scientific examples on account of their overarching importance in physics, chemistry, biology, materials science, industry and nanotechnology; however, we emphasize that the method of neutron scattering, many subareas of which are not mentioned here, can be applied to study a rich variety of other problems including the field of nuclear science and engineering. Furthermore, today, at the doorstep of the 21st century, the scope of neutron-scattering research has already reached a global dimension, as witnessed by the commissioning and construction of a new generation of neutron sources in many regions of the world including the US, European Community, Japan, Korea, China and Austalia as well as the evolving international collaboratives including neutron scattering as one of the key components. We envisage growing activities and exciting advances in neutron science in the coming years.

5. ACKNOWLEDGEMENTS

We would like to thank I. Peral, J.R.D. Copley and D.A. Neumann of the NIST Center for Neutron Research

for their technical support. We are indebted to many collaborators, Christian Burnham (U. of Houston), Melvin Glimcher (Harvard), Alexander Kolesnikov (ANL), Raouf O. Loutfy (MER Corporation), Eugene Mamontov (NIST), Alexander P. Moravsky (MER), Chung-Yuan Mou (National Taiwan U.), M. Ozawa (Nagoya Inst. Tech.), Christian Rey (INP-ENSCT-UPRESA, Toulouse), Nicolas de Souza (ANL), Pappannan Thiyagarajan (ANL) and Jean-Marc Zannoti, (LLB), for their contributions in the course of the studies. We acknowledge the invaluable contribution in experiments involving confined water and for preparing this manuscript by Dr. Li Liu. The work performed at ANL was supported by the U.S. DOE-BES under contract No. W-31-109-ENG-38. Research at MIT is supported by DE-FG02-90ER45429 and 2113-MIT-DOE-591. This work utilized facilities supported in part by the National Science Foundation under Agreement No. DMR-0086210. We benefited from affiliation with EU supported Marie-Curie Research and Training Network on Arrested Matter.

REFERENCES

[1] Y. Oka and S. Koshizuka, J. Nucl. Sci. Tech. **38**, 1081 (2001).
[2] R. Markova,"Investigation on clays for radioactive waste disposal," University of Mining and Geology "St. Ivan Rilski" Annual, Geology and Geophysics, Sofia, Part I. **46**, 379 (2003).
[3] N. Malikova, A. Cadˇ Zne, V. Marry, E. Dubois, P. Turq, J.-M. Zanotti and S. Longeville, Chem. Phys. **317**, 226 (2005).
[4] Methods of Experimental Physcis, edited by K. Skˇsld and D. L. Price (Academic Press, London, 1986), Vol. A-C.
[5] Spectroscopy in Biology and Chemistry: Neutron, X-ray, Laser, edited by S.-H. Chen and S. Yip, (Academic Press, London, 1974).
[6] S.-H. Chen, "Quasi-Elastic and Inelastic Neutron Scattering and Molecular Dynamics of water at Supercooled Temperature," in Hydrogen Bonded Liquids, J. C. Dore, J. Teixeira Eds, Kluwer Academic Publishers, pp 289 (1991).
[7] E. Fratini, S.-H. Chen, P. Baglioni and M.-C. Bellissent-Funel, Phys. Rev. **E 64**, 020201(R) (2001).
[8] E. Fratini, S.-H. Chen, P. Baglioni and M.-C. Bellissent-Funel, J. Phys. Chem. **106**, 158 (2002).
[9] A. Faraone, S.-H. Chen, E. Fratini, P. Baglioni, L. Liu and C. Brown, Phys. Rev. **E 65**, 040501 (2002).
[10] A. Faraone, L. Liu, C.-Y. Mou, P.-C. Shih, J.R.D. Copley and S.-H. Chen, J. Chem. Phys. **119**, 3963 (2003).
[11] L. Liu, A. Faraone, C.-Y. Mou, C.-W. Yen and S.-H. Chen, J. of Phys.: Condensed Matter **16**, S5403 (2004).
[12] M.-C. Bellissent-Funel, S.-H. Chen and J.M. Zanotti, Phys. Rev. E 51, 4558 (1995).
[13] P. Gallo, F. Sciortino, P. Tartaglia and S.-H Chen, Phys. Rev. Lett. **76**, 2730 (1996).
[14] A. Meyer, R. M. Dimeo, P. M. Gehring and D. A. Neumann, Rev. Sci. Instrum. **74**, 2759 (2003).
[15] J. R.D. Copley and J. C. Cook, Chem. Phys. **292**, 477 (2003).
[16] C.-K. Loong et al., Nucl. Instr. Methods **A260**, 381 (1987).
[17] S.H. Lee and P.J. Rossky, J. Chem. Phys. **100**, 3334 (1994).
[18] C. A. Angell, J. Non-Cryst. Solids **131-133**, 13 (1991).
[19] K. Ito, C. T. Moynihan and C. A. Angell, Nature **398**, 492 (1999).
[20] R. Bergman and J. Swenson, Nature **403**, 283 (2000).
[21] P. C. Shih, H. P. Lin and C. Y. Mou, Stud. Surf. Sci. Catal. **146**, 557 (2003).
[22] Y. Liu, W. Zhang, T. J. Pinnavaia, J. Am. Chem. Soc. **122**, 8791 (2000).
[23] R. Ryoo, Sang Hoon Joo and Ji Man Kim, J. Phys. Chem. **B 103**, 7435 (1999).
[24] The MCM-41-S materials are able to withstand prolonged (> 1 month) exposure to water at room temperature without structural decay. Pore size is determined by the capillary condensation in the standard Barrett-Joyner-Halenda (BJH) method in nitrogen adsorption experiment (at 77 K). Because of the uncertainty in estimating the thickness of surface immobile layer, the pore size is a nominal estimation.
[25] R.J. Speedy and C.A. Angell, J. Chem. Phys. **65**, 851 (1976).
[26] S.-H. Chen and M.-C. Bellissent-Funel, in *Hydrogen Bond Networks*, Vol. 435 of *NATO Advances Study Institute, Series C: Mathematical and Physical Sciences*, edited by M.-C. Bellissent-Funel and J.C. Dore, 289 (Kluwer Academic, Dordrecht, 1994).
[27] J.-M. Zanotti, M.-C. Bellissent-Funel and S.-H. Chen, Euro. Phys. Lett. **71**, 91 (2005).
[28] M. Tarek, and D. J. Tobias, Phys. Rev. Lett. **88**, 138101 (2002).
[29] R. M. Lynden-Bell and J. C. Rasaiah, J. Chem. Phys. **105**, 9266 (1996).
[30] M. Settles and W. Doster, Faraday Discuss. Chem. Soc. **103**, 269 (1996).
[31] S.-H. Chen, C. Liao, F. Sciortino, P. Gallo and P. Tartaglia, Phys. Rev. **E 59**, 6708 (1999).
[32] L. Liu, A. Faraone and S.-H. Chen, Phys. Rev. **E 65**, 041506 (2002).
[33] F. Sciortino, P. Gallo, P. Tartaglia and S.-H Chen, Phys. Rev. **E 54**, 6331 (1996).
[34] S.-H. Chen, P. Gallo, F. Sciortino and P. Tartaglia, Phys. Rev. **E 56**, 4231 (1997).
[35] P. Gallo, M. Rovere and E. Spohr, Phys. Rev. Lett. **85**, 4317 (2000).
[36] P. Gallo, M. Rovere and E. Spohr, J. Chem. Phys. **113**, 11324 (2000).
[37] J.M. Zanotti, M.-C. Bellissent-Funel and S.-H. Chen, Phys. Rev. **E 59**, 3084 (1999).
[38] A. Botti, F. Bruni, A. Isopo, M.A. Ricci and A.K. Soper, J. Chem. Phys. **117**, 6196 (2002).
[39] M.J. Benham, J.C. Cook, J.-C. Li, D.K. Ross, P.L. Hall and B. Sarkissian, Phys. Rev. **B 39**, 633 (1989).
[40] C. Rønne, P.-O. Åstrand and S.R. Keiding, Phys. Rev. Lett. **82**, 2888 (1999).
[41] C. Rønne, and S.R. Keiding, J. Mol. Liq. **101**, 199 (2002).
[42] R. Bergman, J. Swenson, L. Børjesson and P. Jacobsson, J. Chem. Phys **113**, 357 (2000).
[43] Y. Ryabov, A. Gutina, V. Archipov and Y. Feldman, J. Phys. Chem. **B 105**, 1845 (2001).
[44] A. Gutina, T. Antropova, E. Rysiakiewicz-Pasek, K. Virnik and Y. Feldman, Microporous and Mesoporous Materials **58**, 237 (2003).
[45] F. D'Orazio, S. Bhattacharja, W.P. Halperin, K. Eguchi and

T. Mizusaki, Phys. Rev. **B 42**, 9810 (1990).
[46] S. Stapf, R. Kimmich and R.-O. Seitter, Phys. Rev. Lett. **75**, 2855 (1995).
[47] J.P. Korb, J.-P. L. Malier, F. Cros, S. Xu and J. Jonas, Phys. Rev. Lett. **77**, 2312 (1996).
[48] R. Holly, H. Peemoeller, C. Choi and M.M. Pintar, J. Chem. Phys. **108**, 4183 (1998).
[49] A. Faraone, L. Liu, C.-Y. Mou, C.-W. Yen and S.-H. Chen, J. Chem. Phys. **121**, 10843 (2004).
[50] P. G. Debenedetti and H. E. Stanley, Physics Today **56**, 40 (June 2003).
[51] M. A. Anisimov, J. V. Sengers and J. M. H. Levelt Sengers, "Near-critical behavior of aqueous systems," in Aquesous Systems at Elevated Temperatures and Pressures: Physical Chemistry in water, Steam and Hydrothermal Solutions, D.A. Palmer, R. Fernandez-Prini and A.H. Harvey (Eds.), 2004 Elsevier Ltd.
[52] Private communication with L. Xu, S. Buldyrev and H. E. Stanley. The authors wish to acknowledge conversations with these researchers on Mar. 27, 2005 when they drew our attention to this interpretation of the TL line.
[53] H. Kanno, R. J. Speedy and C. A. Angell, Science **189**, 880 (1975).
[54] H.E. Stanley, Mysteries of water, M.-C. Bellissent-Funel (Ed.), The Nato Science Series A 305 (1999).
[55] C.A. Angell, S. Borick, and M. Grabow, J. Non-Crys. Sol. **205-207**, 463 (1996).
[56] L. Liu, S.-H. Chen, A. Faraone, C.-W. Yen and C.-Y. Mou, Phys. Rev. Lett. **95**, 117802 (2005).
[57] S. Sastry, C.A. Angell, Nature Materials **2**, 739 (2003).
[58] P. H. Poole, F. Sciortino, U. Essmann, H. E. Stanley, Nature **360**, 324 (1992).
[59] M.A. Ricci, S.-H. Chen, Phys. Rev. **A 34**, 1714 (1986).
[60] A.K. Soper et al., Phys. Rev. Lett. **84**, 2881 (2000).
[61] L. Xu, P. Kumar, S.V. Buldyrev, S.-H. Chen, P. H. Poole, F. Sciortino and H. E. Stanley, Proc. Nat. Acad. Sci. **102**, 16558 (2005).
[62] S. Maruyama et al., AIP conference proc. **708**, 675 (2004).
[63] W. Doster, S. Cusack, W. Petry, Nature (London) **337**, 754-756 (1989); W. Doster, S. Cusack, W. Petry, Phys. Rev. Lett. **65**, 1080 (1990).
[64] B. F. Rasmussen, A. M. Stock, D. Ringe, G. A. Petsko, Nature (London) **357**, 423 (1992).
[65] "Protein-solvent interactions," edited by R. B. Gregory, (Marcel Dekker, New York, 1995).
[66] M. M. Teeter, Annu. Rev. Biophys. Biophys. Chem. **20**, 577 (1991).
[67] J. A. Rupley, P.-H. Yang, G. Tollin, Water in Polymers, ed. Rowland, S. P. Washington D.C.: Am. Chem. Soc. (1980).
[68] I. R. T. Iben, et al. Phys. Rev. Lett. **62**, 1916 (1989).
[69] C. A. Angell, Science **267**, 1924 (1995).
[70] F. Parak, E. W. Knapp, Proc. Natl. Acad. Sci. USA **81**, 7088 (1984).
[71] A. Paciaroni, A. R. Bizzarri, S. Cannistraro, Phys. Rev. **E 60**, R2476 (1999).
[72] G. Caliskan, A. Kisliuk, A. P. Sokolov, J. Non-Crys. Sol. **307-310**, 868 (2002).
[73] P. Kumar, L. Xu, Z. Yan, M. G. Mazza, S. V. Buldyrev, S.-H. Chen, S. Sastry, H. E. Stanley, "Protein Glass Transition and the Liquid-Liquid Critical Point of Water," preprint at http://arxiv.org/abs/cond-mat/0603557.
[74] J. A. Rupley, G. Careri, Protein hydration and function, Advances in Protein Chemistry **41**, 37, edited by C.B. Anfinsen, J.T. Edsall, F.M. Richards and D.S. Eisenberg, (Academic Press, London, 1991).
[75] J. H. Roh, V. N. Novikov, R. B. Gregory, J. E. Curtis, Z. Chowdhuri, A. P. Sokolov, Phys. Rev. Lett. **95**, 038101 (2005).
[76] M. Tarek, D. J. Tobias, Phys. Rev. Lett. **88**, 138101 (2002).
[77] F. Parak, E. N. Frolov, R. L. M¨ossbauer, V. I. Goldanskii, J. Molec. Biol. **145**, 825 (1981).
[78] M. Ferrand, A. J. Dianoux, W. Petry, G. Zaccai, Proc. Nat. Acad. Sci. USA **90**, 9668 (1993).
[79] L. Cordone, M. Ferrand, E. Vitrano, G. Zaccai, Biophys. J. **76**, 1043 (1999).
[80] A. M. Tsai, D. A. Neumann, L. N. Bell, Biophys. J. **79**, 2728 (2000).
[81] H. Lichtenegger, W. Doster, T. Kleinert, A. Birk, B. Sepiol, G. Vogl, Biophys. J. **76**, 414 (1999).
[82] D. Vitkup, D. Ringe, G. A. Petsko, M. Karplus, Nat. Struct. Biol. **7**, 34 (2000).
[83] G. Careri, Prog. Biophys. Mol. Biol. **70**, 223 (1998).
[84] S.-H. Chen, L. Liu, E. Fratini, P. Ganlioni, A. Faraone, E. Mamontov, "Observation of fragile-to-strong dynamic crossover in protein hydration water," submitted to Proc. Nat. Acad. Sci. USA.
[85] E. Mamontov, J. Chem. Phys. **123**, 171101 (2005).
[86] S. Reich, C. Thomsen and J. Maultzsch, Carbon Nanotubes: Basic Concepts and Physical Properties (Cambridge: Wiley-VCH, Weinheim, 2004).
[87] M. Meyyappan, Carbon Nanotubes: Science and Applications (CRC Press, Boca Raton, FL., 2005).
[88] Y. Kong and J. Ma, Proc. Nat. Acad. Sci. USA **98**, 14345 (2001).
[89] A. Kolesnikov, J.-M. Zanotti, C.-K. Loong, P. Thiyagarajan, A. P. Moravsky, R. O. Loutfy and C. J. Burnham, Phys. Rev. Lett. **93**, 35503 (2004).
[90] D. D. Klug and E. Whalley, J. Chem. Phys. **81**, 1220 (1984).
[91] J. C. Li, J. Chem. Phys. **105**, 6733 (1996).
[92] C. J. Burnham and S. S. Xantheas, J. Chem. Phys. **116**, 1500 (2002).
[93] C. J. Burnham and S. S. Xantheas, J. Chem. Phys. **116**, 5115 (2002).
[94] Y. Sugita and Y. Okamoto, Chem. Phys. Lett. **329**, 261 (2000).
[95] K. Koga, G. T. Gao, H. Tanaka and X. C. Zeng, Nature **412**, 802 (2001).
[96] E. Mamontov, C. J. Burnham, S.-H. Chen, A. P. Moravsky, C.-K. Loong, N. R. de Souza and A. I. Kolesnikov, "Mobility of water confined in single- and double-wall carbon nanotubes," J. Chem. Phys. in press (2006).
[97] C.-K. Loong, P. Thiyagarajan, J. Richardson, J. W., M. Ozawa and S. Suzuki, J. Catal. **171**, 498 (1997).
[98] G.-L. Tan and X.-J. Wu, Thin Solid Films **330**, 59 (1998).
[99] J. A. LaVerne, J. Phys. Chem. **B 109**, 5395 (2005).
[100] C.-K. Loong, J. W. Richardson, Jr., and M. Ozawa, J. Catal. **157**, 636 (1995).
[101] E. Mamontov, J. Chem. Phys. **121**, 9087 (2004).
[102] E. Mamontov, J. Chem. Phys. **123**, 024706: 1 (2005).
[103] P. Gallo, m. Rovere, and E. Spohr, J. Chem. Phys. **13**,

11324 (2000).
[104] M. J. Glimcher, "The nature of the mineral phase in bone: Biological and clinical implications", in Metabolic Bone Disease 23-50 (Academic Press, New York, 1998).
[105] C.-K. Loong, C. Rey, L. T. Kuhn, C. Combes, Y. Wu, S.-H. Chen, and M. J. Glimcher, Bone **26**, 599 (2000).
[106] C.-K. Loong and M. Ozawa, J. Electroanal. Chem. **584**, 5 (2005).
[107] G. A. Lager, J. C. Nipko, and C.-K. Loong, Physica B **241-243**, 406 (1998).
[108] G. A. Lager, G. A. Swayze, C.-K. Loong, F. J. Rotella, J. W. Richardson, Jr., and R. E. Stoffregen, Canadian Mineralogist **39**, 1131 (2001).
[109] C.-K. Loong and H. Koyanaka, J. Neut. Res. **13**, 15 (2005).